

General Disclaimer

One or more of the Following Statements may affect this Document

- This document has been reproduced from the best copy furnished by the organizational source. It is being released in the interest of making available as much information as possible.
- This document may contain data, which exceeds the sheet parameters. It was furnished in this condition by the organizational source and is the best copy available.
- This document may contain tone-on-tone or color graphs, charts and/or pictures, which have been reproduced in black and white.
- This document is paginated as submitted by the original source.
- Portions of this document are not fully legible due to the historical nature of some of the material. However, it is the best reproduction available from the original submission.



HIGH FREQUENCY SCATTERING FROM A THIN
LOSSLESS DIELECTRIC SLAB

K. W. Burgener

The Ohio State University

(NASA-CR-162564) HIGH FREQUENCY SCATTERING
FROM A THIN LOSSLESS DIELECTRIC SLAB M.S.
Thesis (Ohio State Univ., Columbus.) 77 p
HC A05/MF A01

N80-14290

CSSL 20N

Unclas

G3/32

46550

The Ohio State University

ElectroScience Laboratory

Department of Electrical Engineering
Columbus, Ohio 43212

Technical Report 710964-4

November 1979

Grant NSG 1498



National Aeronautics and Space Administration
Langley Research Center
Hampton, VA 23365

TECHNICAL REPORT STANDARD TITLE PAGE

1. Report No.		2. Government Accession No.		3. Recipient's Catalog No.	
4. Title and Subtitle HIGH FREQUENCY SCATTERING FROM A THIN LOSSLESS DIELECTRIC SLAB				5. Report Date November 1979	
7. Author(s) K. W. Burgener				6. Performing Organization Code	
9. Performing Organization Name and Address The Ohio State University ElectroScience Laboratory, Department of Electrical Engineering, Columbus, Ohio 43212				8. Performing Organization Report No. ESL 710964-4	
12. Sponsoring Agency Name and Address National Aeronautics & space Administration Langley Research Center Hampton, Virginia 23365				10. Work Unit No.	
15. Supplementary Notes The material contained in this report is also used as a thesis presented to The Ohio State University Graduate School as partial fulfillment for the requirements for the degree Master of Science.				11. Contract or Grant No. Grant NSG 1498	
16. Abstract A high frequency solution for scattering from a thin dielectric slab is developed based on Geometrical Optics and the Geometrical Theory of Diffraction, with the intention of developing a model for a windshield of a small private aircraft for incorporation in an aircraft antenna code. Results of the theory are compared with experimental measurements and Moment Method calculations showing good agreement. Application of the solution is, also, addressed.				13. Type of Report and Period Covered Technical Report	
17. Key Words (Selected by Author(s)) High frequency electromagnetic solution Geometrical Theory of Diffraction Dielectric slab scattering (over)				14. Sponsoring Agency Code	
19. Security Classif. (of this report) Unclassified				18. Distribution Statement	
20. Security Classif. (of this page) Unclassified		21. No. of Pages 73		22. Price*	

*For sale by the Clearinghouse for Federal Scientific and Technical Information, Springfield, Virginia 22151.

17.

Reflection coefficients
Transmission coefficients
Private aircraft
Antenna patterns
Experimental measurements

CONTENTS

Chapter		Page
I	INTRODUCTION.	1
II	TWO-DIMENSIONAL DIELECTRIC STRIP SCATTERING. . .	7
	A. <u>Reflection</u>	9
	B. <u>Transmission</u>	13
	C. <u>Diffraction</u>	15
III	THREE DIMENSIONAL DIELECTRIC SLAB SCATTERING. .	18
IV	RESULTS.	27
	A. <u>Coefficients</u>	27
	B. <u>Dielectric Layer Illuminated by</u> <u>a Rectangular Horn</u>	27
	C. <u>Dipole Illuminating a Dielectric</u> <u>Covered Ground Plane</u>	36
	D. <u>Comparison with Moment Method</u>	57
V	CONCLUSIONS.	71
	REFERENCES.	72

CHAPTER I INTRODUCTION

The heavy and diverse demands on aircraft for commercial, private, and military applications have made the task of the aircraft industry increasingly more complicated. Now millions of dollars must be invested over many years as teams of engineers carefully integrate the many systems involved in a wide-bodied jet or a fighter-bomber. Scale models are built and tested, and plans revised again and again as different possibilities are sorted through to find the few that are feasible and ultimately the one which best meets the demands for application and conditions for production.

One of the systems which the design engineers must integrate into the total aircraft is the antenna system. A poorly functioning antenna on an automobile might result in the minor inconvenience of occasional loss of an AM radio signal. However, a similar loss of signal for an airplane performing an instrument landing could be fatal. Thus the number, type, and locations of antennas to be used is an important question, often made extremely difficult by the complicated nature of the solution of such electromagnetics problems.

At low frequencies where the overall dimensions of the aircraft are on the order of several wavelengths or less, solutions to these problems can be obtained via the method of moments. And for extremely high frequencies, the classical methods of geometrical optics would provide a reasonable approximation. However, for a very wide range of frequencies, typically on the order of 10^9 to 10^{12} Hertz both of these methods of solution break down. Moment method solutions become impractical as the number of unknown currents becomes too large to handle even on a large digital computer, and geometrical optics becomes inaccurate as diffractions become significant. In the past the only practical method of predicting the performance of aircraft antennae in this frequency range was in the building of a scale model in order to experimentally determine its radiation patterns, a costly and time consuming process.

However, recent advances in electromagnetic theory have made this task much simpler. Sommerfeld showed that the solution for a plane wave incident on a perfectly conducting wedge can be expressed as the sum of the geometrical optics wave (V^*) and the diffracted wave (V_B) [1]. And it was Pauli who made possible the expression of (V_B) as an asymptotic series [2]. Further work by many researchers such as Keller [3], and Hutchins and Kouyoumjian [4] lead to the Geometrical Theory of Diffraction (GTD), an asymptotic approximation

to the exact solution for diffractions from certain canonical forms, in the case where the dimensions of the scattering body are on the order of a wavelength or greater.

Research in the GTD and its applications has been carried on at the ElectroScience Laboratory for almost two decades, resulting in increasingly more sophisticated solutions. Several years ago a computer code was developed, basically for far-field radiation patterns of antennae mounted on large commercial aircraft such as the Boeing 737, and delivered to NASA (Langley, Virginia) under Grant No. NGL 36-008-138. The aircraft design engineer was then provided with a relatively fast and efficient method of testing the performance of various antenna configurations. Since that time, improvements and modifications have been made to that code such that it can include greater application and increased efficiency. A major advancement has come about in the development of a new near field pattern solution for the Navy under Contract N00019-77-C-0299.

The question to be dealt with here, dielectric slab scattering, was encountered when this near field code was applied to the study of small private aircraft[5]. Although noteworthy achievements occurred in the modeling of various aircraft appendages such as fuel tanks and engines, this approach broke down in the modeling of a windshield, i.e., the only available solutions were for metallic bodies. For example, Figures 1 and 3 show two possible plate-cylinder models that could be used to analyze the elevation plane pattern of a Cessna 402B. The first assumes a transparent windshield (i.e., reflection coefficient of magnitude zero), and the second a totally reflective windshield (i.e., reflection coefficient of magnitude one). Comparisons of the resulting computed patterns with experimental measurements provided by Melvin Gilreath at NASA (Langley, Virginia) are shown in Figures 2 and 4. Note that the experimental pattern has rather large oscillations in the region from the top backward 30° due to interactions between direct source fields and reflected fields from the windshield, which are not accurately predicted by either of the previous simulations. This results because the reflection coefficient of the windshield is not simply of magnitude zero or unity. In fact it is found to be generally a complex number dependent on the dielectric constant, thickness, frequency, and angle of incidence.

The hypothesis presented here is that modifications may be made to geometrical optics and the GTD to provide accurate solutions for scattering from such dielectric layers. A derivation of the basic theory for reflection, transmission, and diffraction is given along with comparisons of predictions of this theory to known results and a summary.

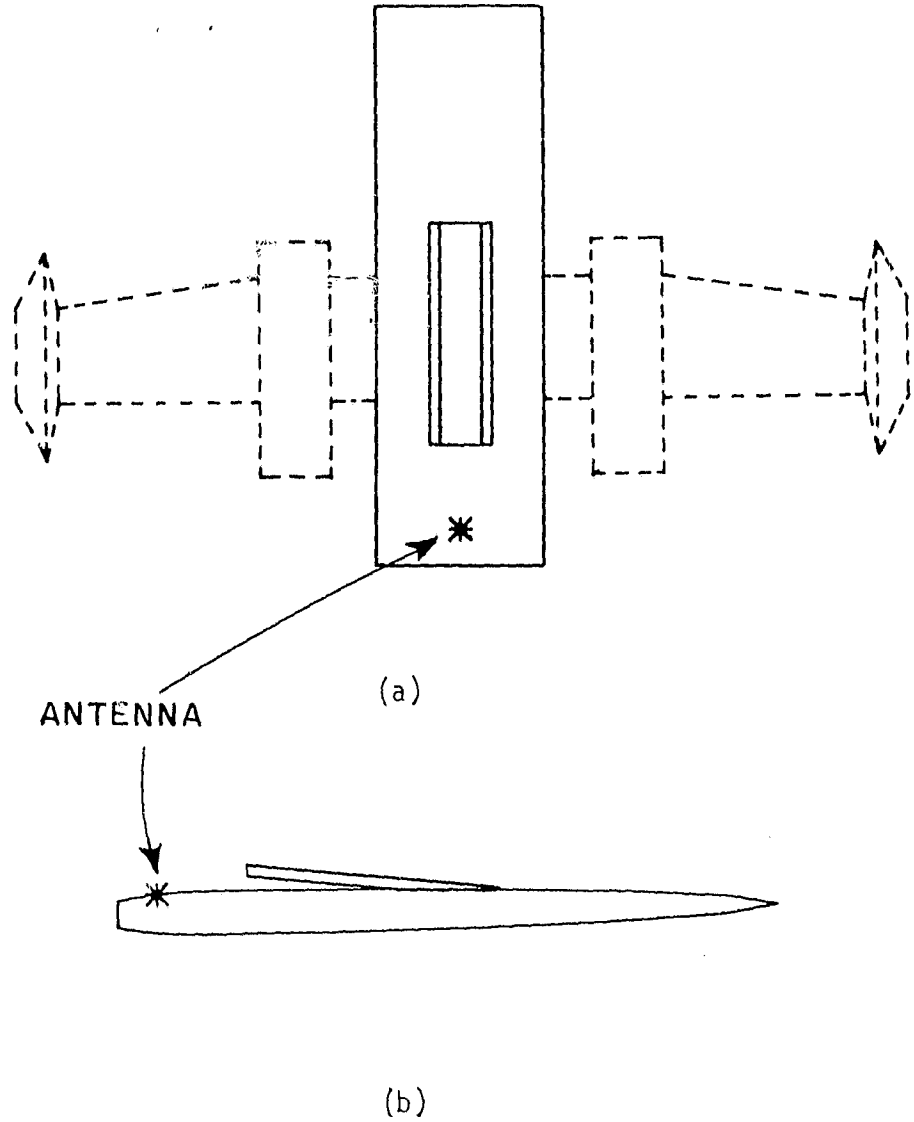


Figure 1. Computer simulation model for Cessna 402B elevation pattern with windshield assumed transparent and monopole antenna mounted forward of the cockpit. (a) top view. (b) side view.

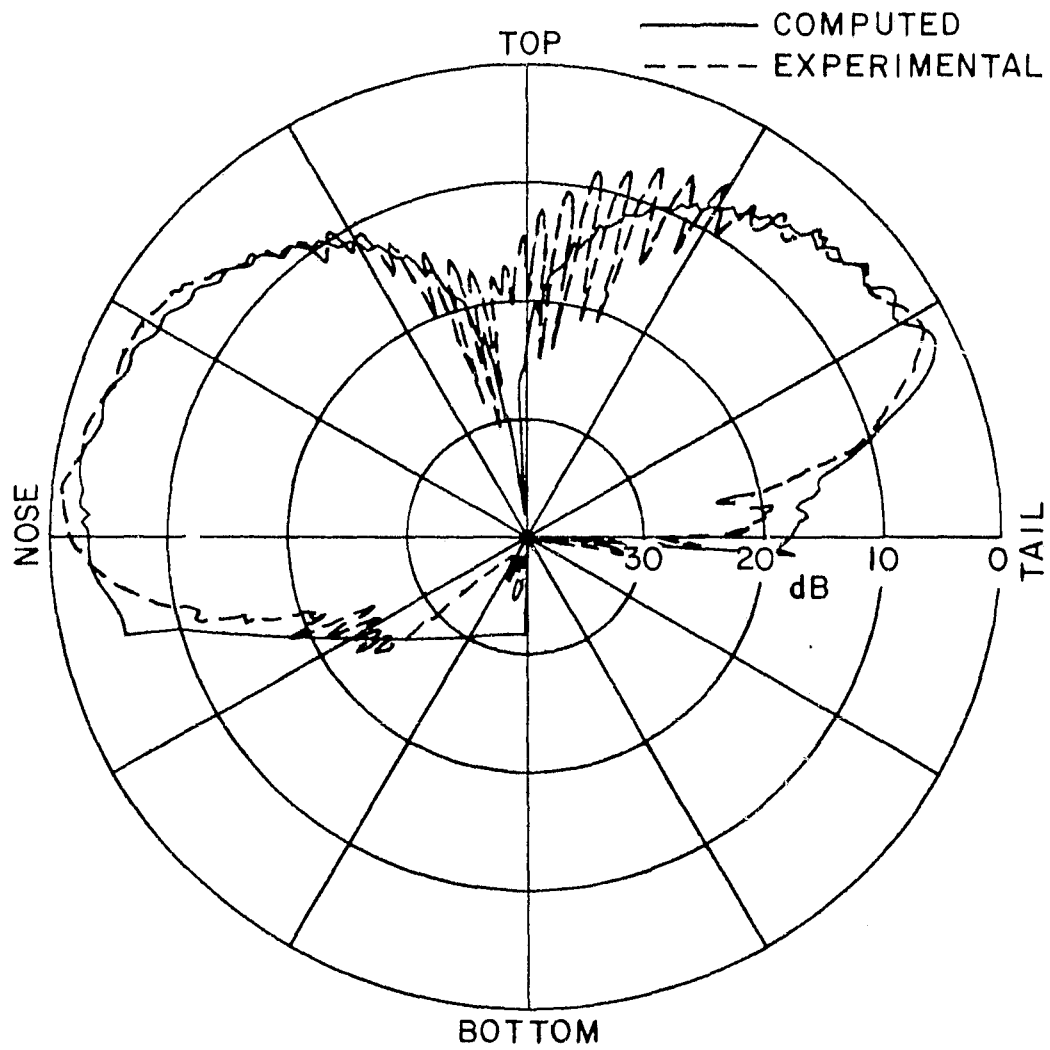


Figure 2. Pattern resulting from Cessna 402B model with transparent windshield shown in Figure 1.

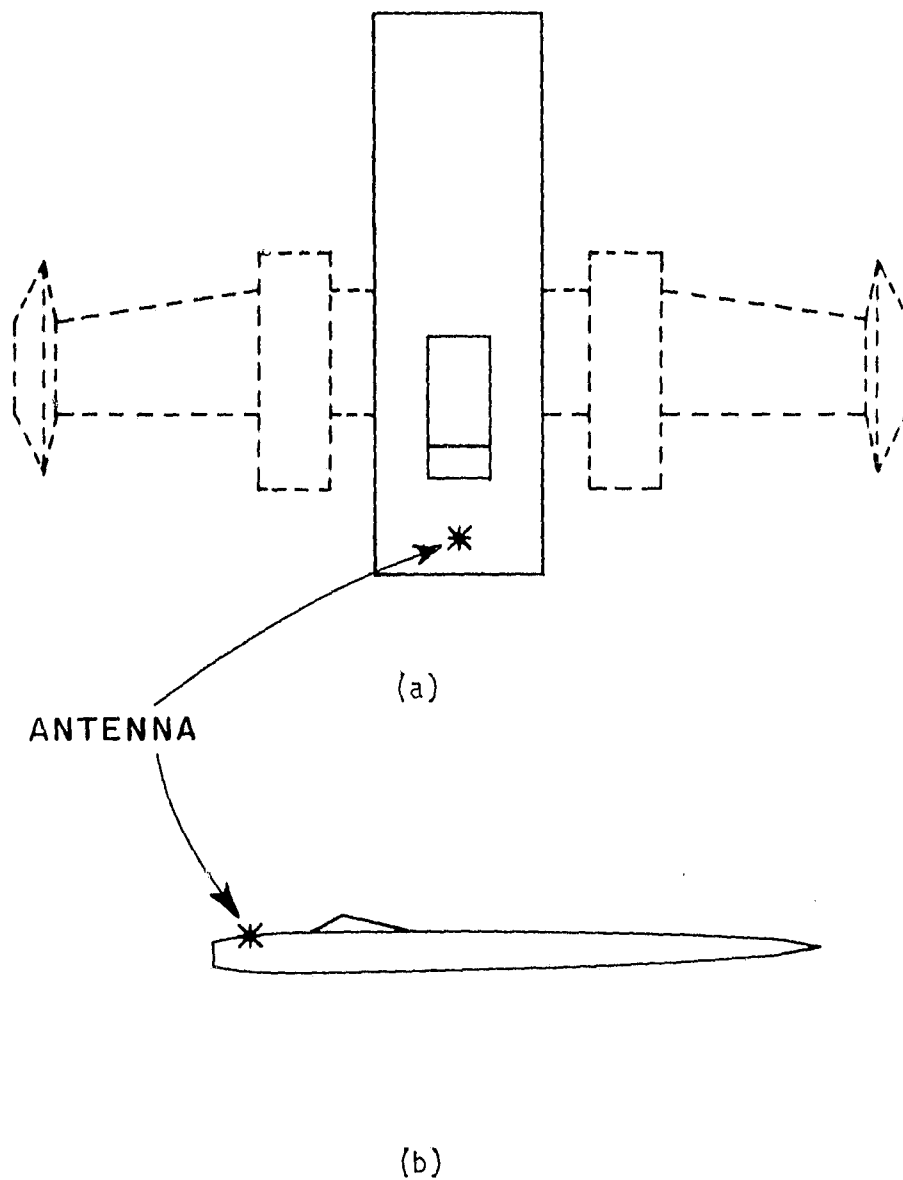


Figure 3. Computer simulation model for Cessna 402B elevation pattern with windshield assumed perfectly conducting and monopole antenna mounted forward of the cockpit. (a) top view. (b) side view.

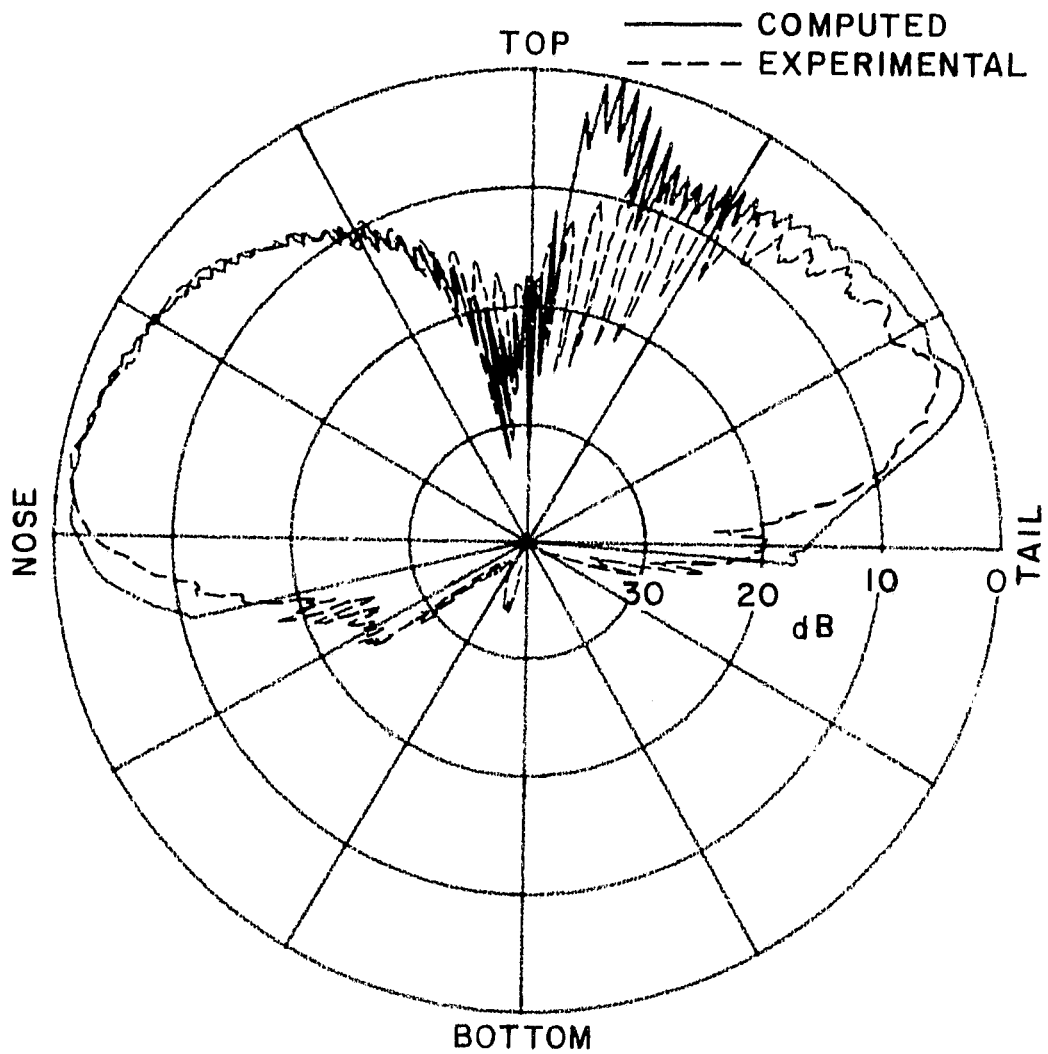


Figure 4. Pattern resulting from Cessna 402B model with perfectly conducting windshield shown in Figure 3.

CHAPTER II
TWO-DIMENSIONAL DIELECTRIC STRIP SCATTERING

Consider the geometry illustrated in Figure 5 with a line source in the presence of a dielectric layer. The dielectric may be of any uniform material and thickness subject to the following restrictions: 1) the diffractions may be assumed to emanate from a single point (Q); 2) energy leaving (Q) tangential to the layer due to a surface wave or transmission through the endface may be ignored; and 3) loss within the layer may be ignored. In light of our goal, a simulation model for an aircraft windshield, these restrictions are not overly severe.

For a metallic half plane the total solution would be composed of incident, reflected, and diffracted fields; however, for the general discussion transmission must also be included. Thus the total electric field at an observation point (P) may be expressed as

$$E^{\text{tot}} = E^i u^i + E^r u^r + E^t u^t + E^d, \quad (1)$$

where u^i , u^r , and u^t are unit step functions shown here explicitly to emphasize the discontinuities in the geometrical optics (G.O.) solution.

The individual terms of Equation (1) may be expressed, assuming a unit magnitude source, as

$$E^i(P) = \begin{cases} \frac{e^{-jks_i}}{\sqrt{s_i}} & \text{Regions I and II} \\ 0 & \text{Region III} \end{cases} \quad (2)$$

$$E^r(P) = \begin{cases} R \frac{e^{-jks_r}}{\sqrt{s_r}} & \text{Region I} \\ 0 & \text{Regions II and III} \end{cases} \quad (3)$$

$$E^t(P) = \begin{cases} 0 & \text{Regions I and II} \\ T \frac{e^{-jks_i}}{\sqrt{s_i}} & \text{Regions III} \end{cases} \quad (4)$$

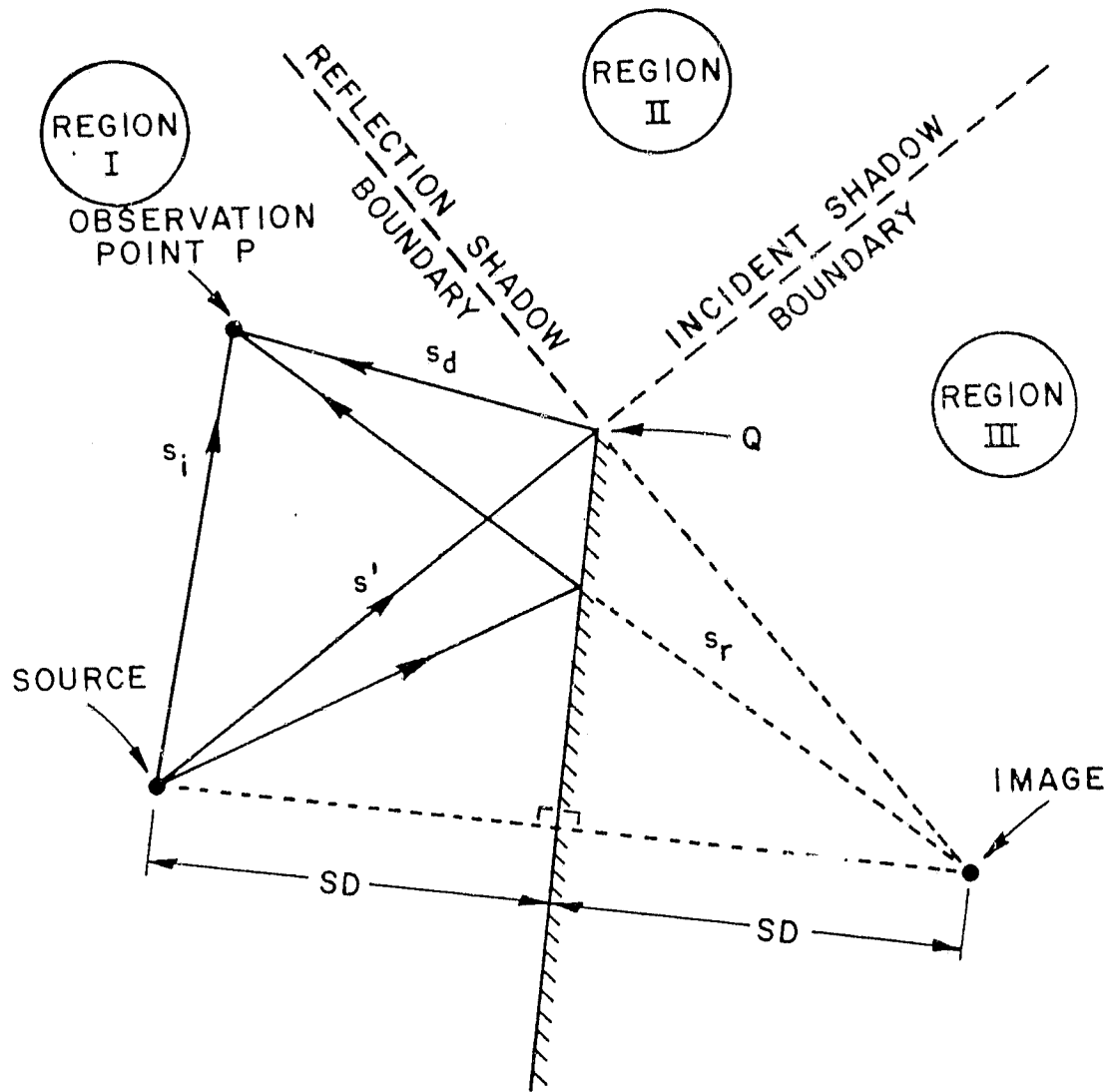


Figure 5. Geometry for half plane scattering discussion.

$$E^d(P) = E^i(Q) D_{s,h} \frac{e^{-jks_d}}{\sqrt{s_{r,i}}} \quad \text{Regions I, II, and III} \quad (5)$$

(Here and throughout an $e^{j\omega t}$ time dependence is assumed and suppressed.) The "R", "T", and "D" are as yet undetermined coefficients of reflection, transmission, and diffraction, respectively. The task now is to determine expressions for these coefficients which when used in Equations (1) through (5) will yield the correct total field for scattering from a dielectric layer. In each case, the results will be stated for a perfectly conducting structure, then extended to include an arbitrary thin dielectric layer.

A. Reflection

If the half plane of Figure 5 is a perfectly conducting structure, the reflection coefficient will be of magnitude one with the sign depending on the polarization of the incident field. Thus,

$$R = \begin{cases} +1 & \text{magnetic line source} \\ -1 & \text{electric line source} \end{cases} \quad (6)$$

for the case of perfect conductivity.

For the more general case, consider a wave propagating in free space incident on a dielectric layer of thickness d and with a dielectric constant ϵ_d as illustrated in Figure 6. At the front face the wave splits, a portion of its energy being reflected and the rest being transmitted into the layer. At the opposite face the transmitted wave again splits, some energy being transmitted out of the dielectric and the rest reflecting back toward the front face. This process continues until all the original energy has left the dielectric, either as part of the total reflection or part of the total transmission.

Thus the total reflection is an infinite sum of waves each of which can be related back to the incident wave provided that a plane wave propagation approximation may be made. Letting R_1 represent the reflection coefficient for the initial external reflection, R_2 represent subsequent internal reflection coefficients, T_1 and T_2 represent transmission coefficients into and out of the layer, respectively, P_d represent the phase delay associated with the field in a single crossing of the slab, and P_a be a term to account for the difference in path length to the observer for different rays leaving the layer in the case of oblique incidence as illustrated in Figure 7, the total reflected field may be expressed as

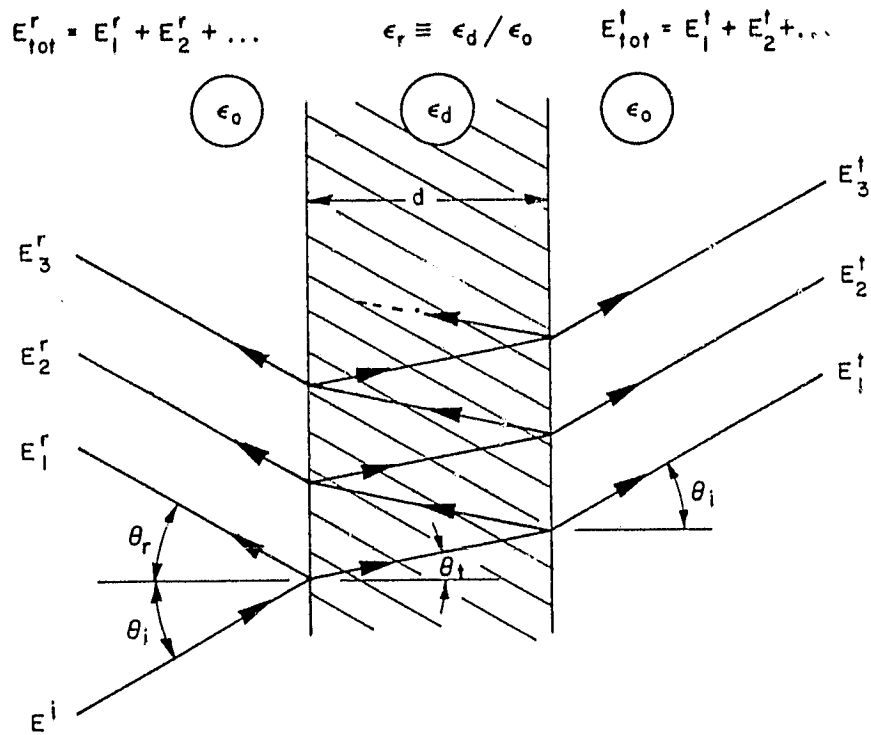


Figure 6. Reflection and transmission for a wave incident on a dielectric slab in free space. Slab assumed of finite thickness but infinite in the other two dimensions.

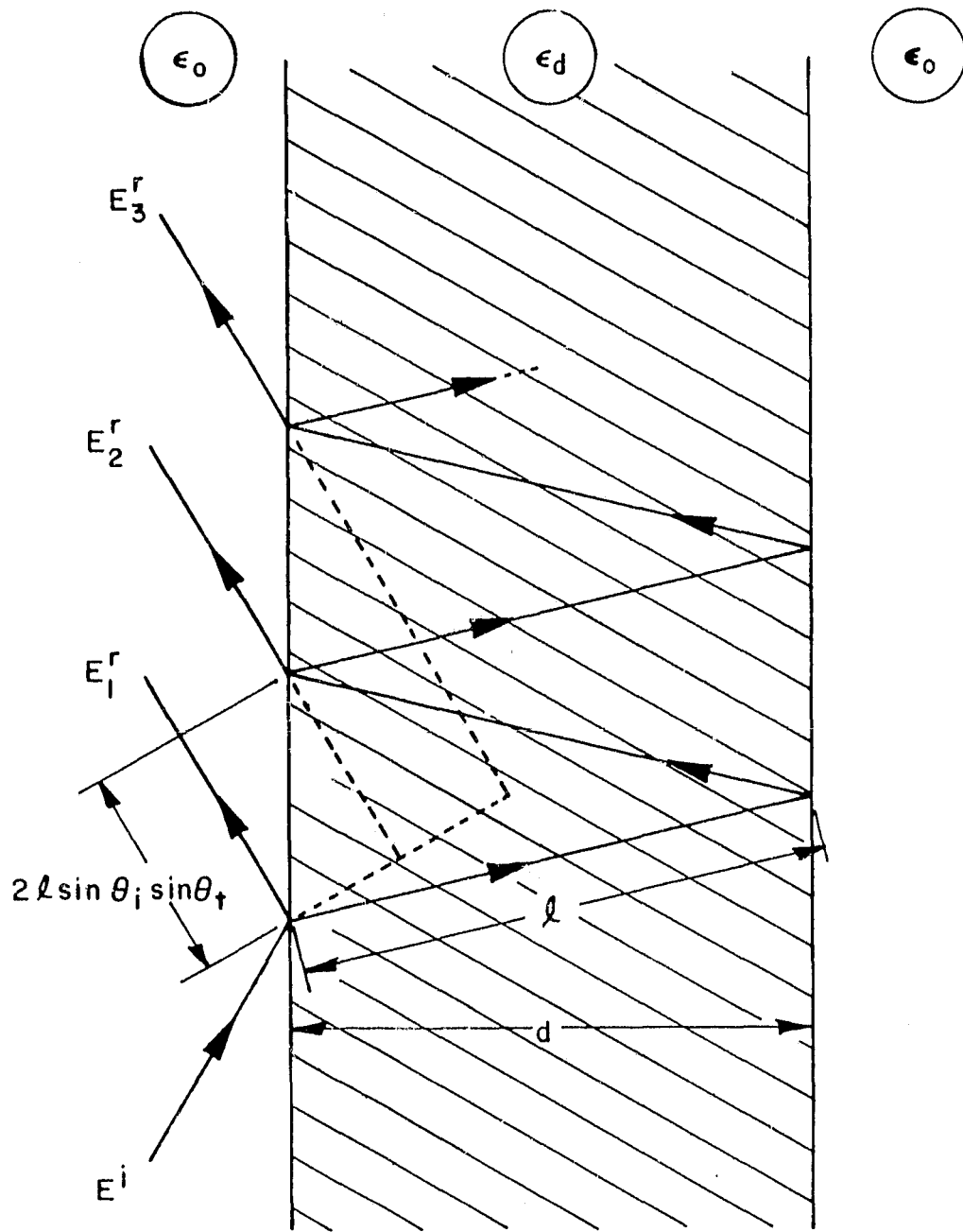


Figure 7. Difference in path length to observer for different rays emerging from slab.

$$E_{\text{tot}}^r = \{R_1 + T_1 T_2 \sum_{n=2}^{\infty} (R_2)^{2n-3} (P_d)^{2n-2} (P_a)^{n-1}\} E^i \quad (7)$$

Use of P_d as in the above equation assumes plane wave propagation within the dielectric. And this usage of P_a assumes that the rays between the slab and the observation point are parallel. These assumptions are satisfied provided that neither the source nor receiver is too close to the slab. These assumptions and some basic trigonometry yield

$$P_d = e^{-jk'\ell} \quad (8)$$

$$P_a = e^{jk2\ell \sin\theta_t \sin\theta_i} \quad (9)$$

where $\ell = d/\cos\theta_t$ and (k) and (k') are the propagation constants for free space and the dielectric medium, respectively. Note that $k' = k\sqrt{\epsilon_r}$, where $\epsilon_r = \epsilon_d/\epsilon_0$.

The coefficients of single reflection and transmission are found via continuity of the tangential components of the \vec{E} and \vec{H} fields, and are given by[6]

$$R_{1(M)} = \frac{\epsilon_r \cos\theta_i - \sqrt{\epsilon_r - \sin^2\theta_i}}{\epsilon_r \cos\theta_i + \sqrt{\epsilon_r - \sin^2\theta_i}} \quad (10a)$$

$$R_{2(M)} = \frac{(1/\epsilon_r) \cos\theta_t - \sqrt{(1/\epsilon_r) - \sin^2\theta_t}}{(1/\epsilon_r) \cos\theta_t + \sqrt{(1/\epsilon_r) - \sin^2\theta_t}} \quad (11a)$$

for the case of a magnetic line source (\vec{E} field parallel to the plane of incidence), and

$$R_{1(E)} = \frac{\cos\theta_i - \sqrt{\epsilon_r - \sin^2\theta_i}}{\cos\theta_i + \sqrt{\epsilon_r - \sin^2\theta_i}} \quad (10b)$$

$$R_{2(E)} = \frac{\cos\theta_t - \sqrt{(1/\epsilon_r) - \sin^2\theta_t}}{\cos\theta_t + \sqrt{(1/\epsilon_r) - \sin^2\theta_t}} \quad (11b)$$

for the case of an electric line source (\vec{E} field perpendicular to the plane of incidence). In both cases one finds

$$T_1 = R_1 + 1 \quad (12)$$

$$T_2 = R_2 + 1 \quad (13)$$

$$\theta_r = \theta_i \quad (14)$$

$$\sin \theta_t = \sin \theta_i / \sqrt{\epsilon_r} \quad (15)$$

Through the evaluation of the geometrical series and noting that $R_2 = -R_1$, Equation (7) may be simplified to the desired total reflection coefficient:

$$R_{(M,E)} = \frac{R_1(M,E)(1 - P_d^2 P_a)}{1 - R_1^2(M,E) P_d^2 P_a} \quad (16)$$

B. Transmission

Referring again to Figure 5, one finds for a perfectly conducting half plane that $T = 0$. For the dielectric case, however, the transmitted field is once again an infinite sum and may be expressed as

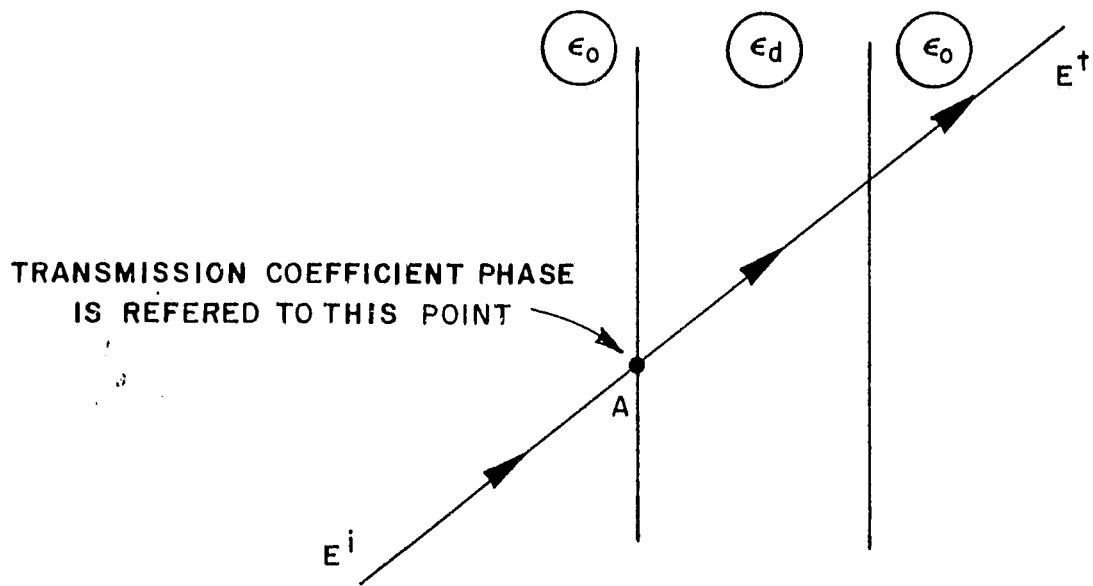
$$E_{tot}^t = \{T_1 T_2 P_t \sum_{n=1}^{\infty} (P_d)^{2n-1} (P_a)^{n-1} (R_2)^{2n-2}\} E^i, \quad (17)$$

where E^i is the field that would have been incident on the receiver in the absence of the dielectric layer. Here P_t is a term to cause the transmission coefficient to act as a simple modification of the incident field as shown in Figure 8(a). Note that without this term the phase is referred to point (B) in Figure 8(b). This term is given by

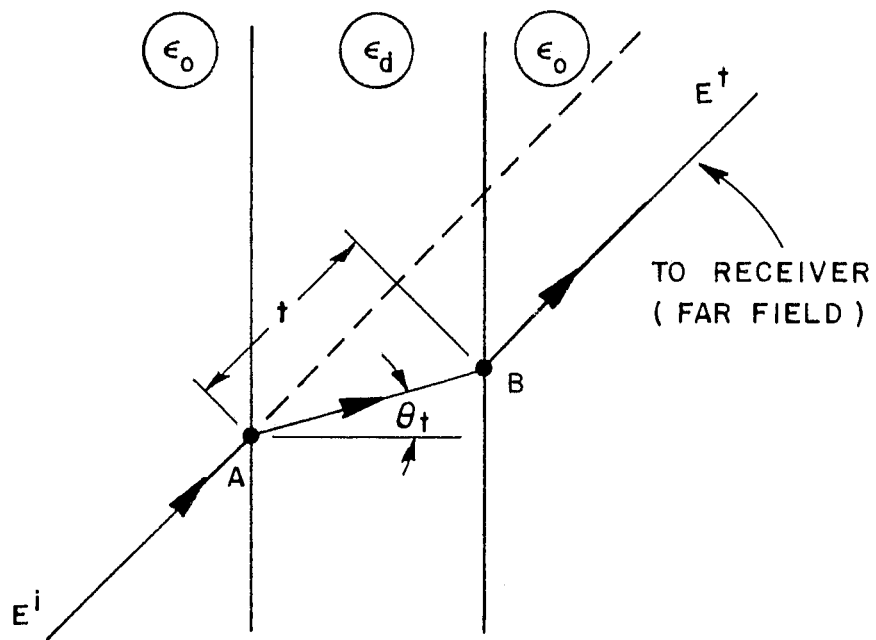
$$P_t = e^{jk \ell \cos(\theta_i - \theta_t)} \quad (18)$$

As before in the case of reflection, much simplification is possible. After some manipulation one arrives at the desired total transmission coefficient:

$$T_{(M,E)} = \frac{(1 - R_1^2(M,E)) P_d P_t}{1 - R_1^2(M,E) P_d^2 P_a} \quad (19)$$



a) Assumed path.



b) An actual path.

Figure 8. Transmitted ray paths.

C. Diffraction

Consider the geometry illustrated in Figure 9 which shows a wave incident on a perfectly conducting wedge, one of the canonical forms for which the Geometrical Theory of Diffraction (GTD) provides an asymptotic solution. The diffraction coefficient for the 2D case is generally given by

$$D = \begin{cases} D_h & \text{magnetic line source} \\ D_s & \text{electric line source,} \end{cases} \quad (20)$$

where the "h" and "s" subscripts refer to acoustically "hard" (\vec{E} field perpendicular to diffracting edge) and "soft" (\vec{E} field parallel to diffracting edge) diffractions, respectively. Reference [7,8] gives these coefficients for a half plane ($n=2$ in Figure 9) as

$$D_{s,h}(\phi, \phi'; \beta_0) = - \frac{e^{-j \frac{\pi}{4}}}{2\sqrt{2\pi k} \sin \beta_0} \left\{ \frac{F[kLa(\phi - \phi')]}{\cos\left(\frac{\phi - \phi'}{2}\right)} \mp \frac{F[kLa(\phi + \phi')]}{\cos\left(\frac{\phi + \phi'}{2}\right)} \right\}, \quad (21)$$

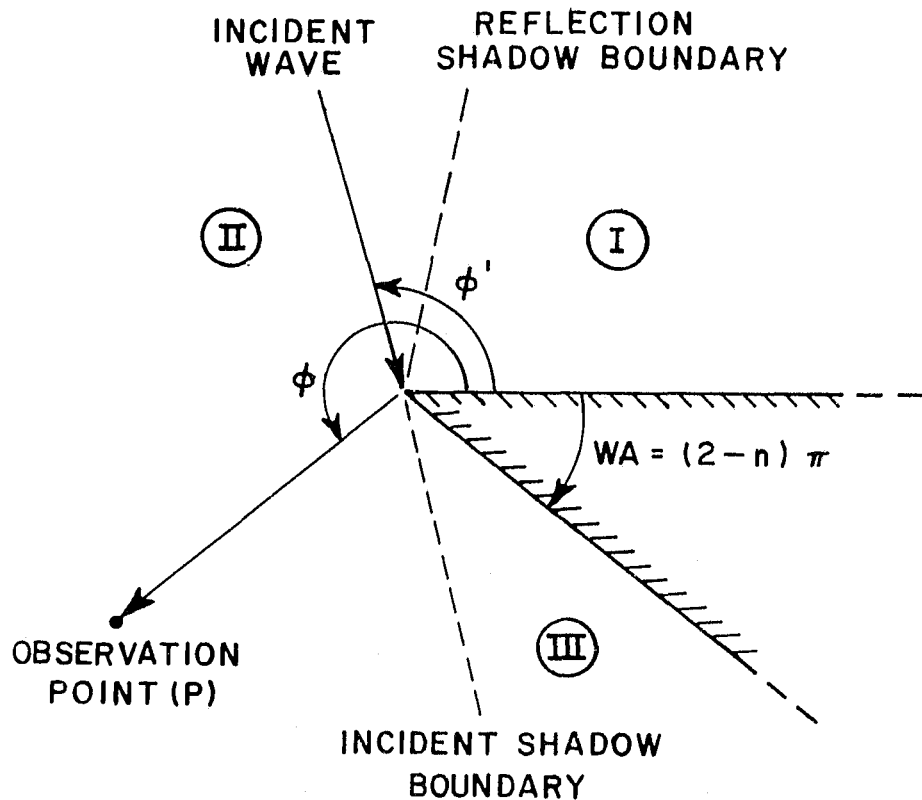


Figure 9. Geometry for perfectly conducting wedge diffraction.

where

$$F(X) = 2j\sqrt{X} e^{jX} \int_{\sqrt{X}} e^{-j\tau^2} d\tau.$$

Often the notation

$$D_{s,h}(\phi, \phi') = D(\phi - \phi') \mp D(\phi + \phi') \quad (22)$$

where

$$D(\phi \pm \phi') = \frac{-e^{-j\frac{\pi}{4}}}{2\sqrt{2\pi k \sin\beta_0}} \frac{F[kLa(\phi \pm \phi')]}{\cos\left(\frac{\phi \pm \phi'}{2}\right)}$$

is used. This form shows explicitly how the GTD coefficients compensate for each of the two discontinuities in the G.O. solution. The $D(\phi - \phi')$ term is associated with the incident shadow boundary and the $D(\phi + \phi')$ term is associated with the reflection shadow boundary.

Note that in the application of Equation (22) one would use the (-) sign for the case of an electric line source and the (+) sign for the case of a magnetic line source. Thus the "R" of Equation (6) may be incorporated here, and the diffracted field written as

$$E^d(P) = E^i(Q) [D(\phi - \phi') + R D(\phi + \phi')] \frac{e^{-jks_d}}{\sqrt{s_d}} \quad (23)$$

Note that for the perfectly conducting case the discontinuity at the incident shadow boundary is unity times the incident field near the boundary and the coefficient of $D(\phi - \phi')$ is unity; likewise, the discontinuity at the reflection shadow boundary is R times the reflected field near that boundary and the coefficient of $D(\phi + \phi')$ is R.

As the subject of attention is now shifted to diffractions from dielectrics, the discussion must be limited to flat layers rather than wedges since uniform thickness was a requirement for derivation of the reflection and transmission coefficients. As noted above, there is a correlation between the magnitude of the discontinuity at each shadow boundary and the coefficient of the corresponding $D(\phi \pm \phi')$ term. In the dielectric case the discontinuity at the reflection shadow boundary is again related to R, although R is no longer simply -1; at the incident shadow boundary the discontinuity is (1-T) times the incident field, which reduces to unity for the metallic case. Therefore, it is conjectured that the diffraction coefficient for a finite dielectric layer is given by

$$D = [(1-T)D(\phi - \phi') + R D(\phi + \phi')] \quad (24)$$

The values of "R" and "T" are given by Equations (16) and (19) with θ_i being the angle between the ray incident on the diffraction edge and the normal to the reflecting face.

Equations (16), (19), and (24), when used in Equations (1) through (5) give the desired solution for the problem shown in Figure 5. This has been demonstrated experimentally as will be discussed in Chapter IV. However, before presenting this confirmation, the theory will be expanded to the more general three dimensional case.

CHAPTER III
THREE DIMENSIONAL DIELECTRIC SLAB SCATTERING

In the previous chapter coefficients were developed for the various terms in the G.O.-GTD solution for two dimensional scattering from a finite dielectric layer. These coefficients are still valid in the more general case, however, care must be taken in their application. In treating 3D problems one must keep in mind two facts: 1) spherical waves are being considered rather than cylindrical waves, and 2) the field can be arbitrarily polarized rather than merely that of a simple electric or magnetic line source. The first of these facts means that the spreading factors become more complicated than e^{-jk_s}/\sqrt{s} ; the second means one must find a suitable coordinate system in which to express the resulting fields, transforming coordinates as necessary to apply the coefficients of the previous chapter.

It will be convenient at this point to introduce the "ray fixed coordinate system." Letting \hat{n} be the unit vector normal to the slab, \hat{I} be the incident unit vector from the source to a point on the slab, and \hat{R} be the reflection unit vector from the point of reflection to the observation point, one may define the following:

$$\begin{aligned}\hat{u}_{\perp} &= \hat{n} \times \hat{I}, \\ \hat{u}_{\parallel}^i &= \hat{I} \times \hat{u}_{\perp}, \\ \hat{u}_{\parallel}^r &= \hat{R} \times \hat{u}_{\perp},\end{aligned}$$

where (\perp) and (\parallel) indicate vectors perpendicular and parallel, respectively, to the ordinary plane of incidence, the plane containing \hat{I} and \hat{n} . These unit vectors form the orthogonal bases for the ray fixed coordinate system as illustrated in Figure 10. The field of a ray traveling in the direction of \hat{I} or \hat{R} is now completely specified by its components E_{\perp} and E_{\parallel} . Note that E_{\perp}^i corresponds to the 2D case of an electric line source and E_{\parallel}^i corresponds to the 2D case of a magnetic line source. In the ray fixed system one may utilize the coefficients of the previous chapter and express the reflected and transmitted fields in the following manner:

$$\begin{bmatrix} E_{\parallel}^r \\ E_{\perp}^r \end{bmatrix} = \begin{bmatrix} R_{(M)} & 0 \\ 0 & R_{(E)} \end{bmatrix} \begin{bmatrix} E_{\parallel}^i \\ E_{\perp}^i \end{bmatrix} f_r(s) \quad (28)$$

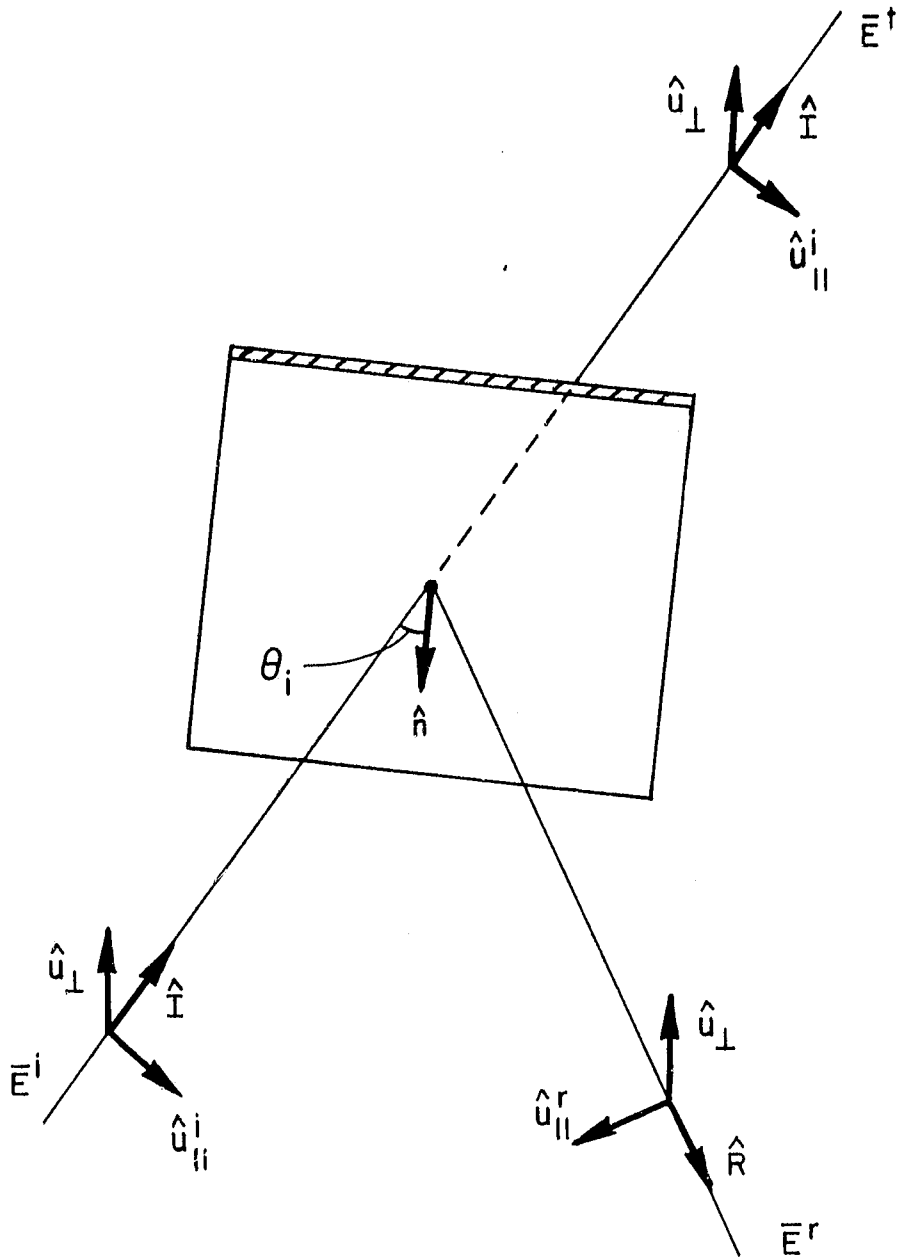


Figure 10. Ray fixed coordinate system used for 3D reflection and transmission.

$$\begin{bmatrix} E_{II}^t \\ E_I^t \end{bmatrix} = \begin{bmatrix} T_{(M)} & 0 \\ 0 & T_{(E)} \end{bmatrix} \begin{bmatrix} E_{II}^i \\ E_I^i \end{bmatrix} f_t(s) \quad (29)$$

The angle of incidence to be used in computing the coefficients is given by

$$\theta_i = \cos^{-1}(-\hat{I} \cdot \hat{n}) \quad (30)$$

The spreading factor for the transmitted field is the same as that for an incident field,

$$f_t(s) = \frac{e^{-jks}}{s} \quad (31)$$

For the reflected field the spreading factor is slightly more complicated, given by [8]

$$f_r(s) = \frac{\sqrt{\frac{r_1 r_2}{(\rho_1^r + s)(\rho_2^r + s)}}}{(\rho_1^r + s)(\rho_2^r + s)} e^{-jks} \quad (32)$$

The ray fixed coordinate system, although ideal for reflection and transmission problems, is not suitable for the diffraction solution. The diffraction coefficients presented in the previous chapter are valid only when the incident field is expressed by components parallel and perpendicular to the edge fixed plane of incidence, the plane containing the incident ray and the diffracting edge; and the diffracted field expressed by components parallel and perpendicular to the edge fixed plane of diffraction, which contains the diffracted ray and the edge. Thus the "edge fixed coordinate system" is introduced and illustrated in Figure 11. Letting \hat{e} be the unit vector parallel to the diffracting edge, \hat{I} be the incident unit vector from the source to the diffraction point (Q_E), and \hat{D} be the diffraction unit vector from (Q_E) to the observation point (P), one may define the following:

$$\hat{\phi}' = -\hat{e} \times \hat{I}, \quad (33)$$

$$\hat{\beta}'_0 = \hat{\phi}' \times \hat{I}, \quad (34)$$

$$\hat{\phi} = \hat{e} \times \hat{D}, \quad \text{and} \quad (35)$$

$$\hat{\beta}_0 = \hat{\phi} \times \hat{D}. \quad (36)$$

These vectors form the two orthonormal bases of the edge fixed coordinate system. Note that the ordinary plane of incidence intersects the edge fixed plane of incidence along the incident ray, and

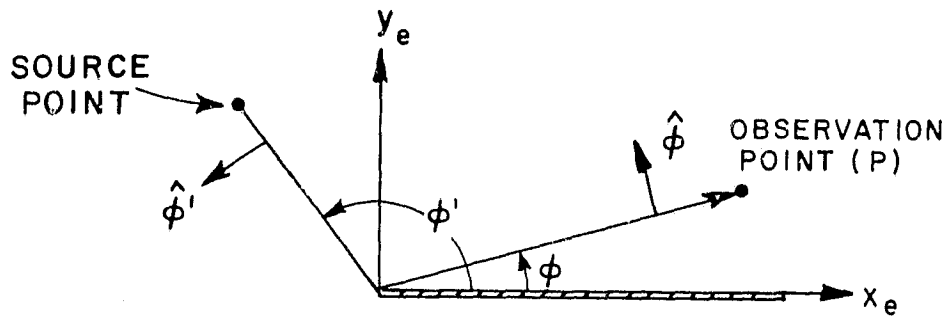
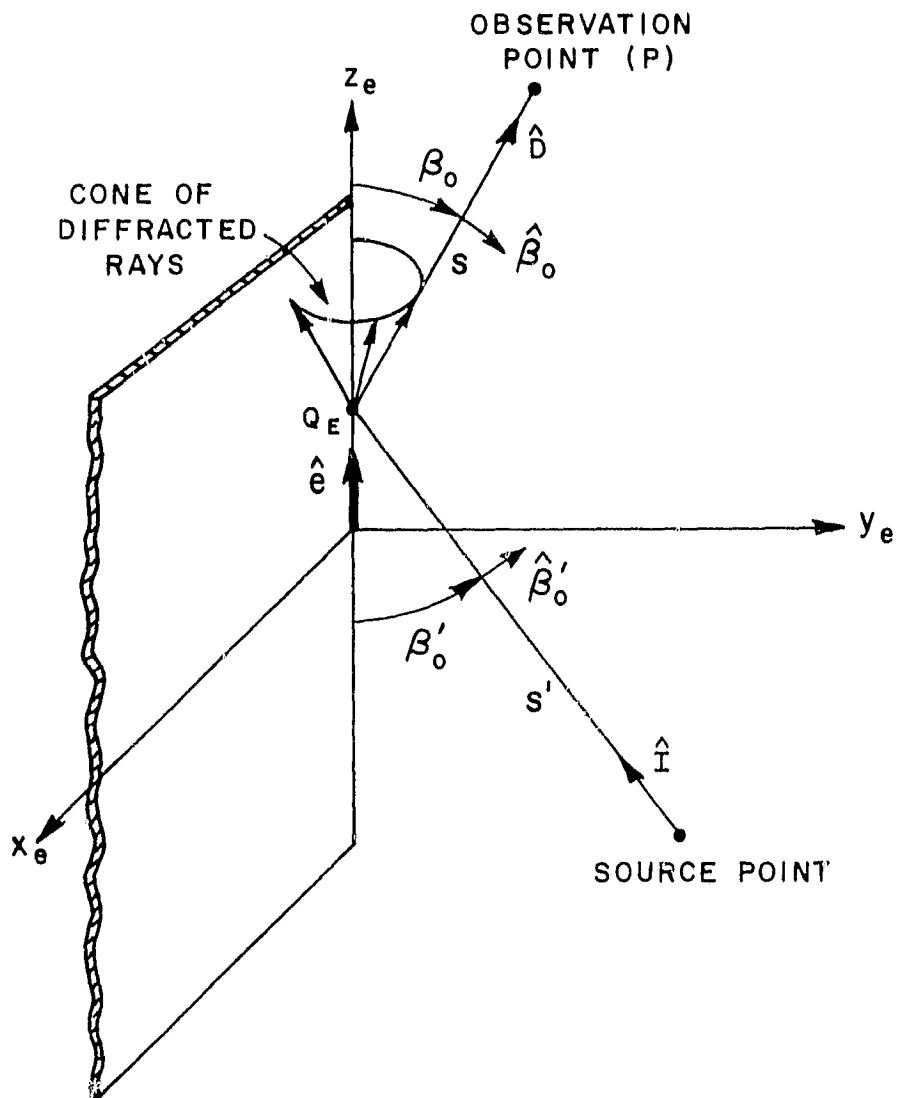


Figure 11. Edge fixed coordinate system used for 3D diffraction.

the edge fixed plane of diffraction along the diffracted ray. The relationship between these planes, and thus the relationship between the ray fixed system and the edge fixed system is depicted in Figure 12. It can be shown [8] that the angles α and α_i , defined as shown in Figure 12 are related by $\alpha_i = -\alpha$.

It is apparent that the incident field may be expressed in the edge fixed coordinate system as

$$E_{\beta_0}^i = E_{\parallel}^i \cos\alpha - E_{\perp}^i \sin\alpha \quad (37a)$$

$$E_{\phi}^i = E_{\parallel}^i \sin\alpha + E_{\perp}^i \cos\alpha \quad (37b)$$

These expressions may be written more compactly in matrix notation as

$$E_{e.f.}^i = T(-\alpha)E^i, \quad (38)$$

where

$$T(-\alpha) = \begin{bmatrix} \cos\alpha & -\sin\alpha \\ \sin\alpha & \cos\alpha \end{bmatrix} \quad (39)$$

Likewise the reflected field is transformed between systems by

$$E_{\beta_0}^r = E_{\parallel}^r \cos\alpha + E_{\perp}^r \sin\alpha \quad (40a)$$

$$E_{\phi}^r = -E_{\parallel}^r \sin\alpha + E_{\perp}^r \cos\alpha \quad (40b)$$

This may be expressed as

$$E_{e.f.}^r = T(\alpha)E^r, \quad (41)$$

where

$$T(\alpha) = \begin{bmatrix} \cos\alpha & \sin\alpha \\ -\sin\alpha & \cos\alpha \end{bmatrix} \quad (42)$$

In the edge fixed system, the 3D diffracted field may be expressed in a manner analogous to the 2D case by

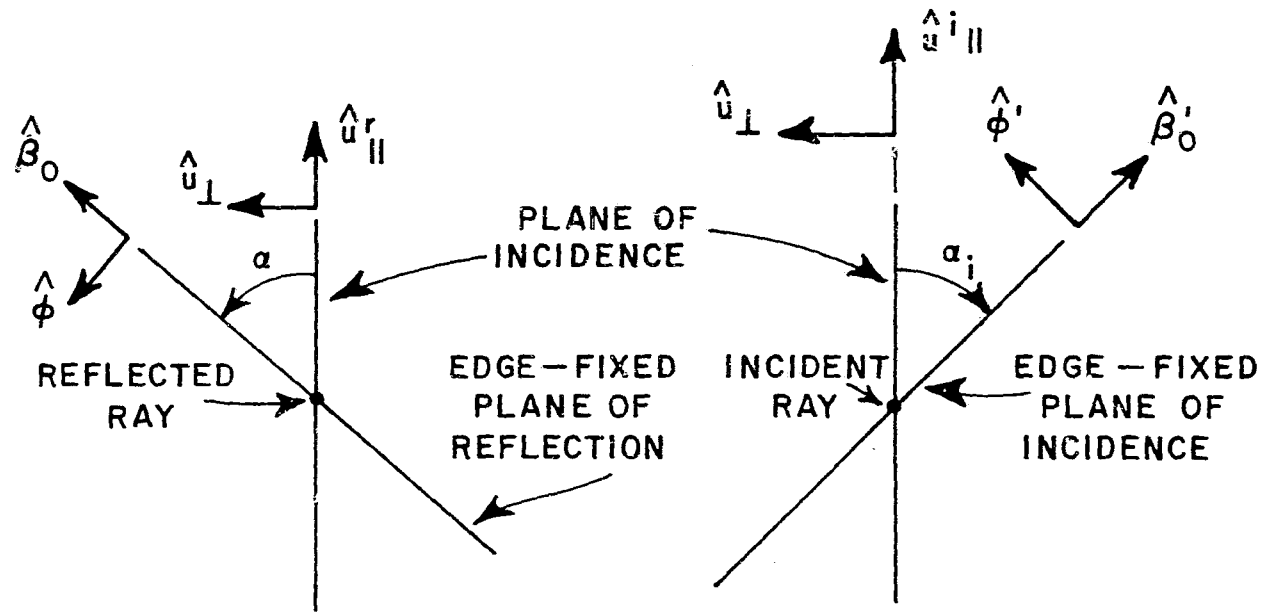


Figure 12. Comparison of the ray fixed coordinate system and the edge fixed coordinate system. The incident and reflected rays are perpendicular to the page and directed outward.

$$\begin{bmatrix} E_{\beta_0}^d \\ E_{\phi}^d \end{bmatrix} = \left[\bar{A} D(\phi-\phi') + \bar{B} D(\phi+\phi') \right] \begin{bmatrix} E_{\beta_0}^i \\ E_{\phi'}^i \end{bmatrix} \sqrt{\frac{s'}{s(s'+s)}} e^{-jks} \quad (43)$$

where the matrices \bar{A} and \bar{B} serve the same function of scaling the $D(\phi \pm \phi')$ terms to the proper complex value of the discontinuity as did (R) and $(1-T)$ in the 2D case. \bar{A} is the polarization matrix associated with the discontinuity in the G.O. field at the incident shadow boundary and \bar{B} the polarization matrix associated with the discontinuity at the reflection shadow boundary. However, these discontinuities must be expressed in terms of the unit vectors $\hat{\beta}_0, \hat{\phi}$.

On the lit side of the incident shadow boundary one finds (see Figure 11)

$$\begin{bmatrix} E_{\beta_0}^i \\ E_{\phi}^i \end{bmatrix} = - \begin{bmatrix} E_{\beta_0}^i \\ E_{\phi'}^i \end{bmatrix} \quad (44)$$

On the side not directly illuminated by the source, the transmitted field is present. To express this one must start with E^i in the edge fixed system, transform to the ray fixed system in which the transmission coefficients are valid, perform the transmission operation, then transform back to the edge fixed system. Thus the field in this region is given by

$$\begin{bmatrix} E_{\beta_0}^t \\ E_{\phi}^t \end{bmatrix} = -T(-\alpha) \begin{bmatrix} T_{(M)} & 0 \\ 0 & T_{(E)} \end{bmatrix} T^{-1}(-\alpha) \begin{bmatrix} E_{\beta_0}^i \\ E_{\phi'}^i \end{bmatrix} \quad (45)$$

So the total discontinuity is given by

$$\left\{ - \begin{bmatrix} 1 & 0 \\ 0 & 1 \end{bmatrix} + \begin{bmatrix} \cos\alpha & -\sin\alpha \\ \sin\alpha & \cos\alpha \end{bmatrix} \begin{bmatrix} T_{(M)} & 0 \\ 0 & T_{(E)} \end{bmatrix} \begin{bmatrix} \cos\alpha & \sin\alpha \\ -\sin\alpha & \cos\alpha \end{bmatrix} \right\} \begin{bmatrix} E_{\beta_0}^i \\ E_{\phi'}^i \end{bmatrix}$$

such that

$$\bar{A} = \begin{bmatrix} -1 + T_{(M)} \cos^2\alpha + T_{(E)} \sin^2\alpha & (T_{(M)} - T_{(E)}) \sin\alpha \cos\alpha \\ (T_{(M)} - T_{(E)}) \sin\alpha \cos\alpha & -1 + T_{(M)} \sin^2\alpha + T_{(E)} \cos^2\alpha \end{bmatrix} \quad (46)$$

REPRODUCIBILITY OF THE
ORIGINAL PAGE IS POOR

Likewise at the reflection shadow boundary one notes that

$$\begin{bmatrix} E_{\beta_0}^r \\ E_{\phi}^r \end{bmatrix} = T(\alpha) \begin{bmatrix} R_{(M)} & 0 \\ 0 & R_{(E)} \end{bmatrix} T^{-1}(-\alpha) \begin{bmatrix} E_{\beta_0}^i \\ E_{\phi'}^i \end{bmatrix} \quad (47)$$

Therefore the discontinuity is given by

$$\left\{ \begin{bmatrix} \cos\alpha & \sin\alpha \\ -\sin\alpha & \cos\alpha \end{bmatrix} \begin{bmatrix} R_{(M)} & 0 \\ 0 & R_{(E)} \end{bmatrix} \begin{bmatrix} \cos\alpha & \sin\alpha \\ -\sin\alpha & \cos\alpha \end{bmatrix} \right\} \begin{bmatrix} E_{\beta_0}^i \\ E_{\phi'}^i \end{bmatrix}$$

such that

$$\bar{B} = \begin{bmatrix} R_{(M)} \cos^2\alpha - R_{(E)} \sin^2\alpha & (R_{(M)} + R_{(E)}) \sin\alpha \cos\alpha \\ -(R_{(M)} + R_{(E)}) \sin\alpha \cos\alpha & -R_{(M)} \sin^2\alpha + R_{(E)} \cos^2\alpha \end{bmatrix} \quad (48)$$

For computational purposes, the 3D diffracted field is written as

$$\begin{bmatrix} E_{\beta_0}^d \\ E_{\phi}^d \end{bmatrix} = \begin{bmatrix} -D_a & -D_b \\ -D_c & -D_d \end{bmatrix} \begin{bmatrix} E_{\beta_0}^i \\ E_{\phi'}^i \end{bmatrix} \sqrt{\frac{s'}{s(s'+s)}} e^{-jks} \quad (49)$$

where

$$D_a = (1 - T_{(M)} \cos^2\alpha - T_{(E)} \sin^2\alpha) D(\phi - \phi') - (R_{(M)} \cos^2\alpha - R_{(E)} \sin^2\alpha) D(\phi + \phi') \quad (50)$$

$$D_b = -(T_{(M)} - T_{(E)}) \sin\alpha \cos\alpha D(\phi - \phi') - ((R_{(M)} + R_{(E)}) \sin\alpha \cos\alpha) D(\phi + \phi') \quad (51)$$

$$D_c = -(T_{(M)} - T_{(E)}) \sin\alpha \cos\alpha D(\phi - \phi') + ((R_{(M)} + R_{(E)}) \sin\alpha \cos\alpha) D(\phi + \phi') \quad (52)$$

$$D_d = (1 - T_{(M)} \sin^2\alpha - T_{(E)} \cos^2\alpha) D(\phi - \phi') + (R_{(M)} \sin^2\alpha - R_{(E)} \cos^2\alpha) D(\phi + \phi'). \quad (53)$$

The total 3D solution for scattering from a dielectric slab is now complete, given by the sum of Equations (28), (29), and (49). In the next chapter, computed patterns are compared to experimental results for confirmation of the theory.

CHAPTER IV RESULTS

REPRODUCIBILITY OF THE
ORIGINAL PAGE IS POOR

A. Coefficients

Plots showing the variation of the reflection and transmission coefficients of Chapter II with respect to the dielectric layer thickness are shown in Figures 13(a) and 13(b), respectively. These results are for a typical dielectric (polystyrene) illuminated by a plane wave with normal incidence ($\theta_i = 0^\circ$ in Figure 6). In the evaluation of the reflection coefficient, one would expect the first two terms in the series to dominate. These two terms will differ in phase by the propagation length of two transversals of the layer plus a 180° phase shift due to the R_2 reflection off the back face. Thus a maximum is anticipated at the points where $D/\lambda = (2n+1)/4$ with $n=1,2,3,\dots$, which is the case of the propagation phase delay plus the reflection phase change equaling an integral multiple of 360° , i.e., the first two terms of the series adding in phase. A minimum would be expected when these terms add out of phase, which occurs at $D/\lambda = n/2$. Both predictions match the results shown in Figure 13.

In the transmission case, the second term has two R_2 reflections, which add a 360° phase change. Thus the phase difference between the two dominant terms is effectively caused by the propagation of two layer transversals. Thus maxima occur at $D/\lambda = n/2$ and minima at $D/\lambda = (2n+1)/4$. These again match the computed results shown in Figure 13.

B. Dielectric Layer Illuminated by a Rectangular Horn

For purposes of an initial testing of the theory in a real world situation it is applied to the problem shown in Figure 14, where the pattern is measured in the E plane of the horn with the phase origin at the center of the horn aperture. A corresponding simulation model made use of the above theory for scattering from the polyethylene. The horn was treated as a set of magnetic line sources (one at the apex and one at each of the diffracting edges) as in the corner reflector model presented in Reference [9]. The first measurements were taken with the horn alone, and the results at various frequencies are shown in Figures 15 through 19. Since only the main beam of the horn will interact with the dielectric, and only these interactions are of interest, extreme care was not taken in the setup of the horn.

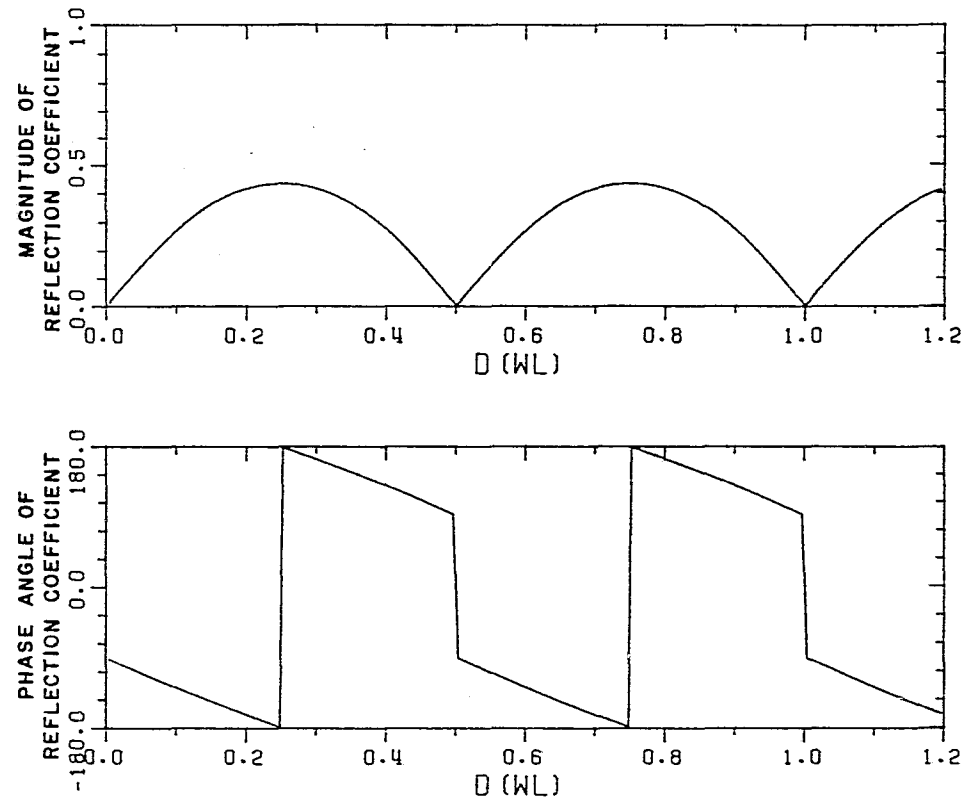


Figure 13a. Plot of reflection coefficient vs. slab thickness for normal incidence on a polystyrene slab ($\epsilon_r=2.55$) with the E field normal to the plane of incidence. Note that "D" is measured in wavelengths within the dielectric.

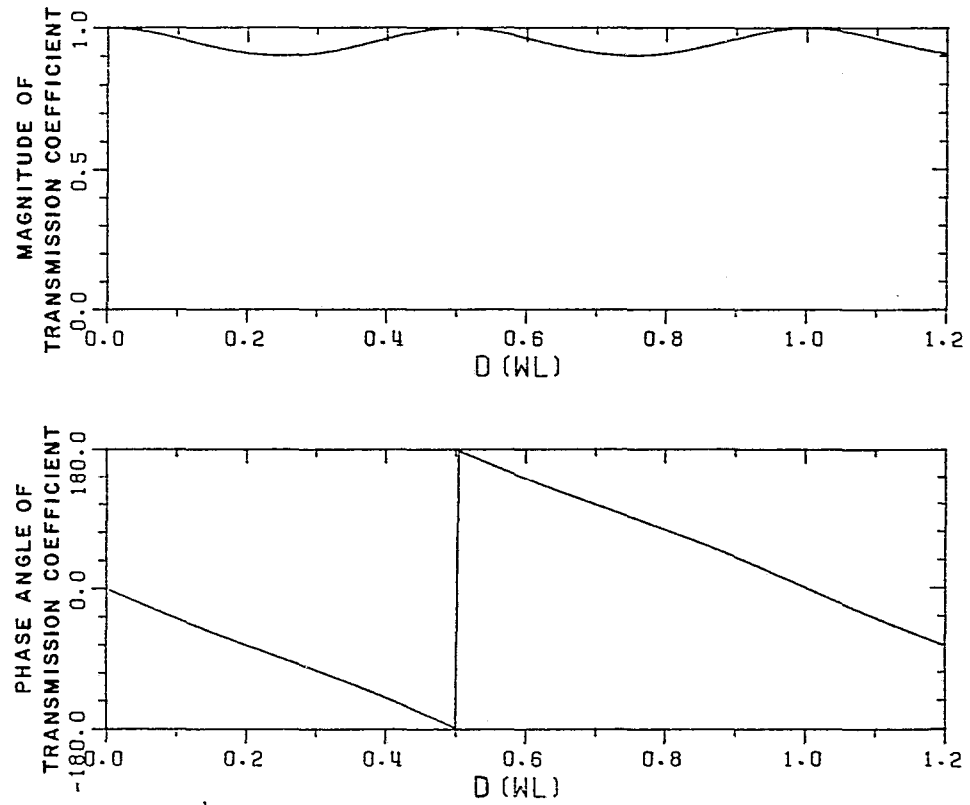


Figure 13b. Plot of transmission coefficient vs. slab thickness for normal incidence on a polystyrene slab ($\epsilon_r=2.55$) with the E field normal to the plane of incidence. D is measured in wavelengths within the dielectric.

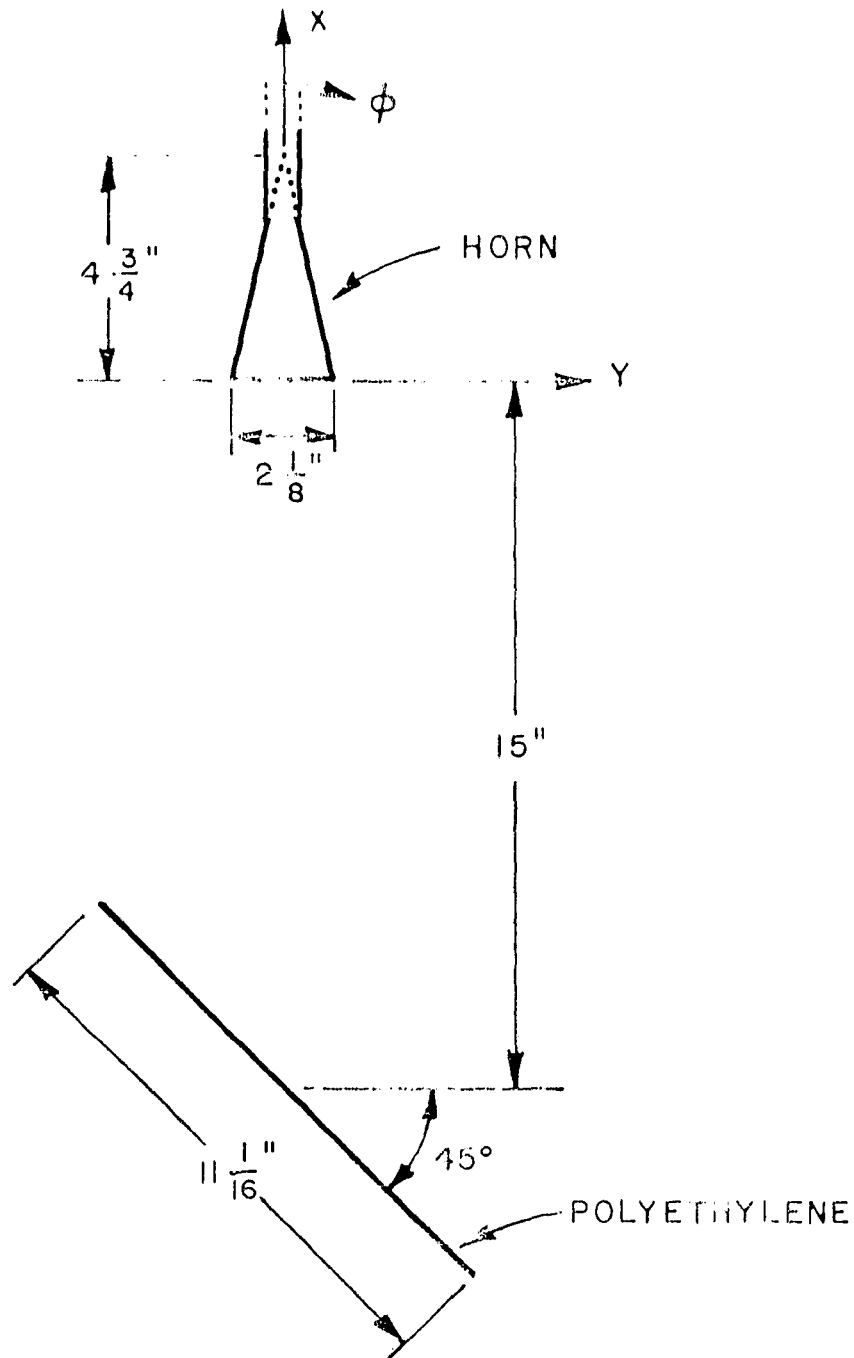


Figure 14. Polyethylene geometry used to test scattering theory. Measurements are taken in the E plane of the horn. Polyethylene thickness is .1285" and $\epsilon_r = 2.25$ at 10 GHz. A standard gain horn manufactured by Narda Corp. is used.

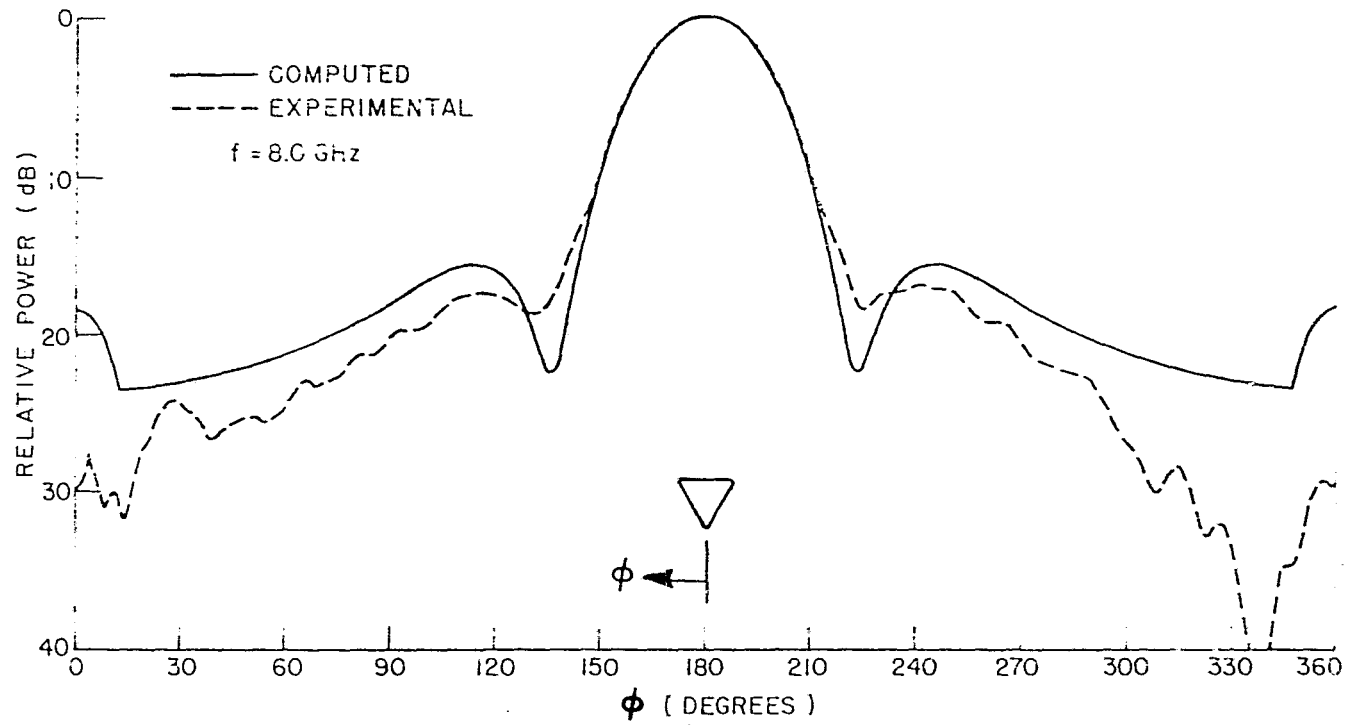


Figure 15. E-plane horn pattern at 8.0 GHz.

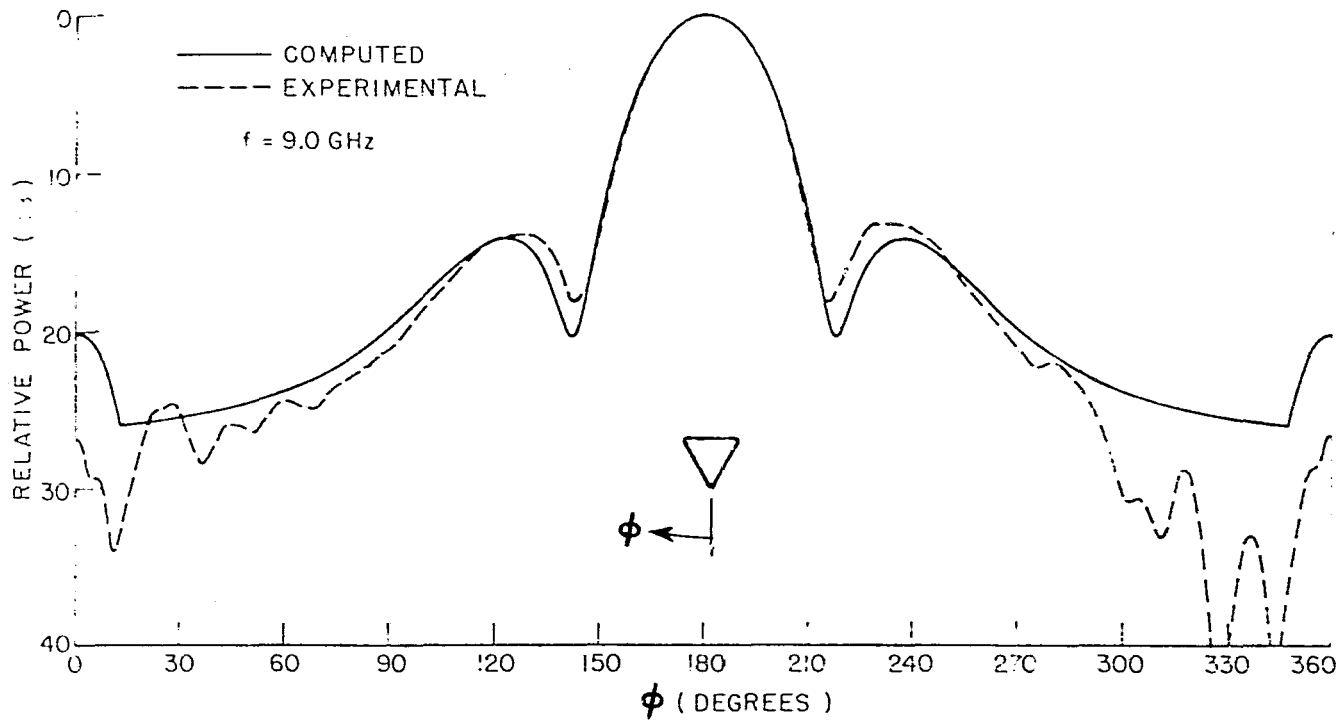


Figure 16. E-plane horn pattern at 9.0 GHz.

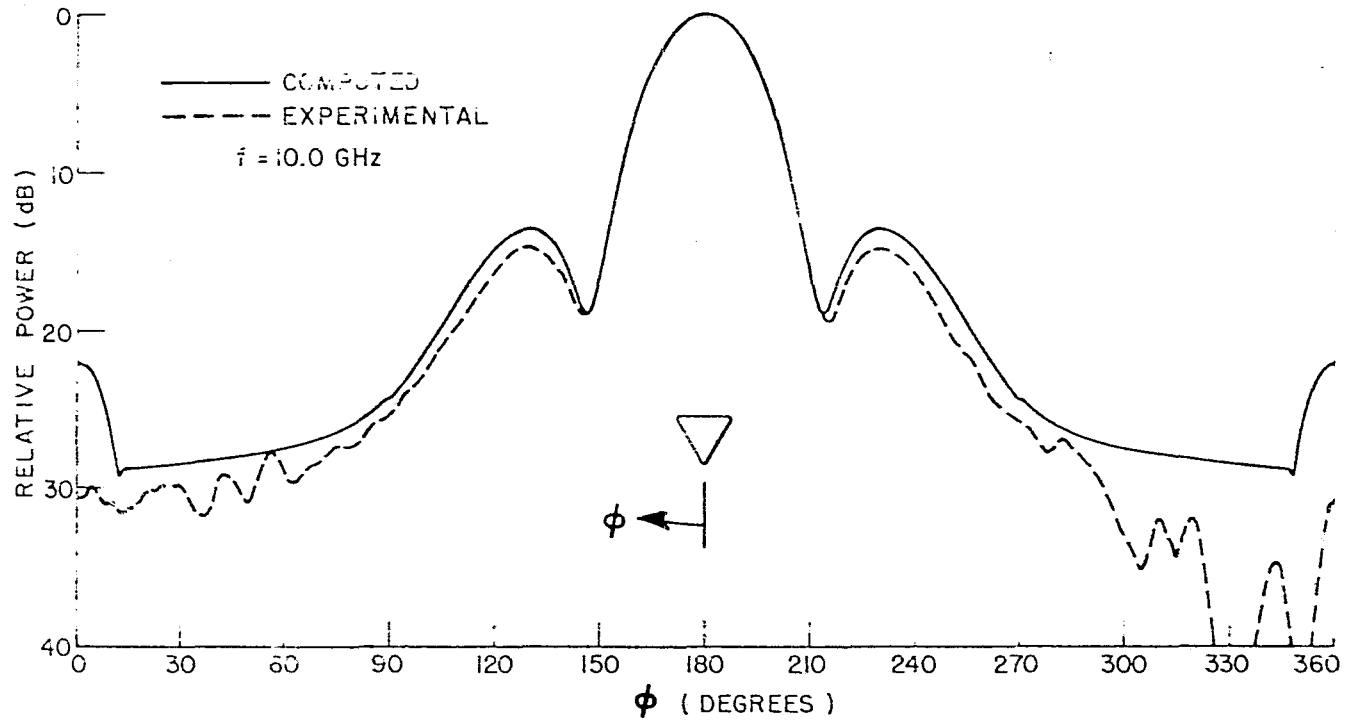


Figure 17. E-plane horn pattern at 10.0 GHz.

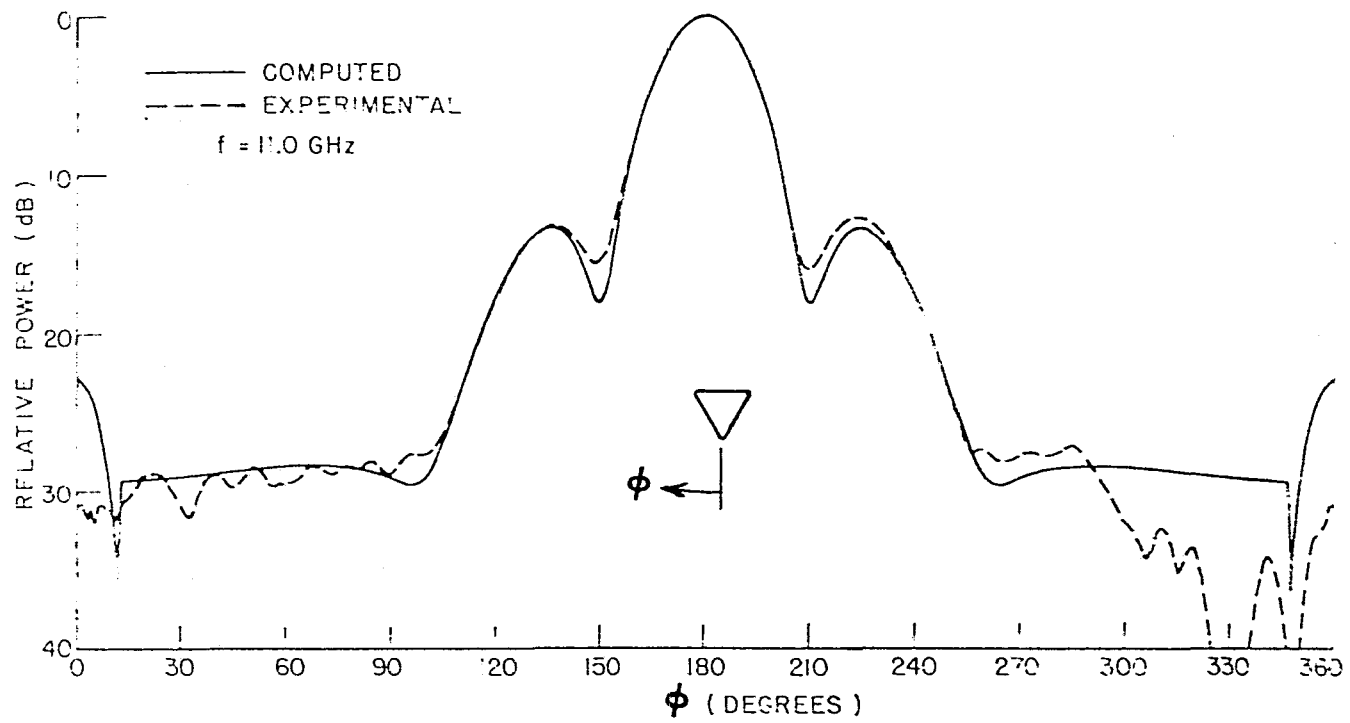


Figure 18. E-plane horn pattern at 11.0 GHz.

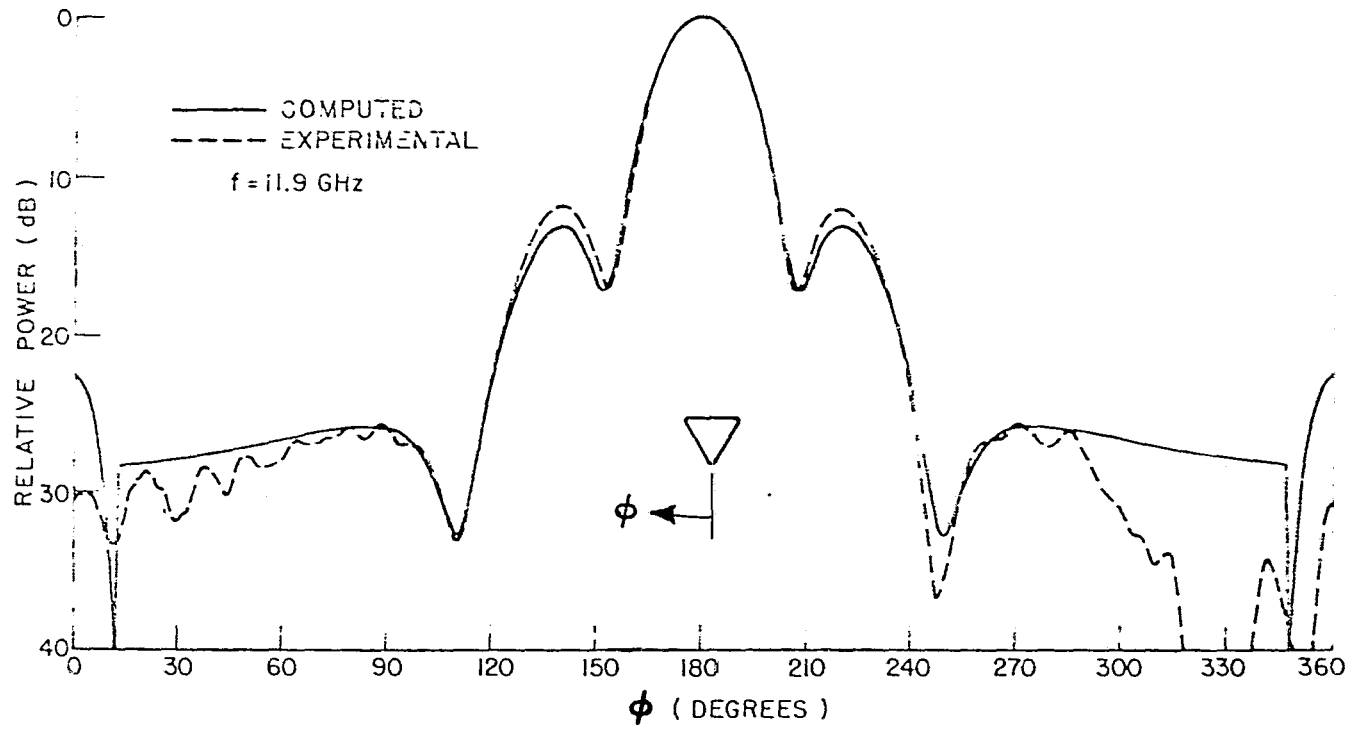


Figure 19. E-plane horn pattern at 11.9 GHz.

This accounts for much of the difficulties in the back region of the horn, especially 0° to 60° and 300° to 360° . Most notably, the measured patterns are not symmetrical. However, in all cases the main beam is in good agreement with the computed results. This, as will be seen, is sufficient for the testing of the theory.

Results for the entire geometry illustrated in Figure 14 are shown in Figures 20-24 for various frequencies. Again difficulties are observed in the region behind the horn, 0° to 60° and 300° to 360° ; however, these can be attributed to the experimental setup rather than the dielectric solution, which is the subject of investigation at present. For confirmation of the theory, one should look to the two areas of the pattern most strongly affected by the dielectric, i.e., the area of direct transmission around $\phi=180^\circ$ and the area of direct reflection around $\phi=90^\circ$. In these two areas one finds the results quite acceptable. The shape of the main beam, which is determined totally by transmitted and diffracted fields, is at all frequencies found to be in good agreement. In addition, the reflection region shows good results. Here ripple is produced by interactions between the horn sidelobes and scattering from the dielectric. The amplitude and frequency of this ripple agree reasonably well with the measured ripple in each case.

Figure 25 shows a second geometry used for verification of the dielectric scattering theory. Here the slab is much thicker and of slightly higher dielectric constant. Also it is closer to the horn which will reduce the spacial frequency of pattern ripple, making it easier to compare results. Calculated and measured patterns shown in Figures 26-28 for various frequencies agree well in overall shape, especially in the main beam and reflection regions.

Figure 29 shows another geometry with the same slab as the previous problem placed perpendicular to the horn axis. In this case the region of primary interest is the main beam around $\phi=180^\circ$, determined completely by transmitted and diffracted fields. The calculated and measured patterns illustrated in Figures 30-34 show reasonably good agreement in each case.

C. Dipole Illuminating a Dielectric Covered Ground Plane

The geometry illustrated in Figure 35 shows a test of the theory using a dipole source rather than a horn, and with the dielectric slab backed by a ground plane. Here the calculated results are found by a re-derivation of the coefficients of Chapter II setting the coefficient for reflections from the second face equal to -1 , and the experimental measurements were obtained by measuring the pattern in the planes defined by the z axis and each of the dashed lines of Figure 35. Results are shown in Figures 36 and 37 for the principal planes and Figures 38 and 39 for the two polarizations of the diagonal pattern.

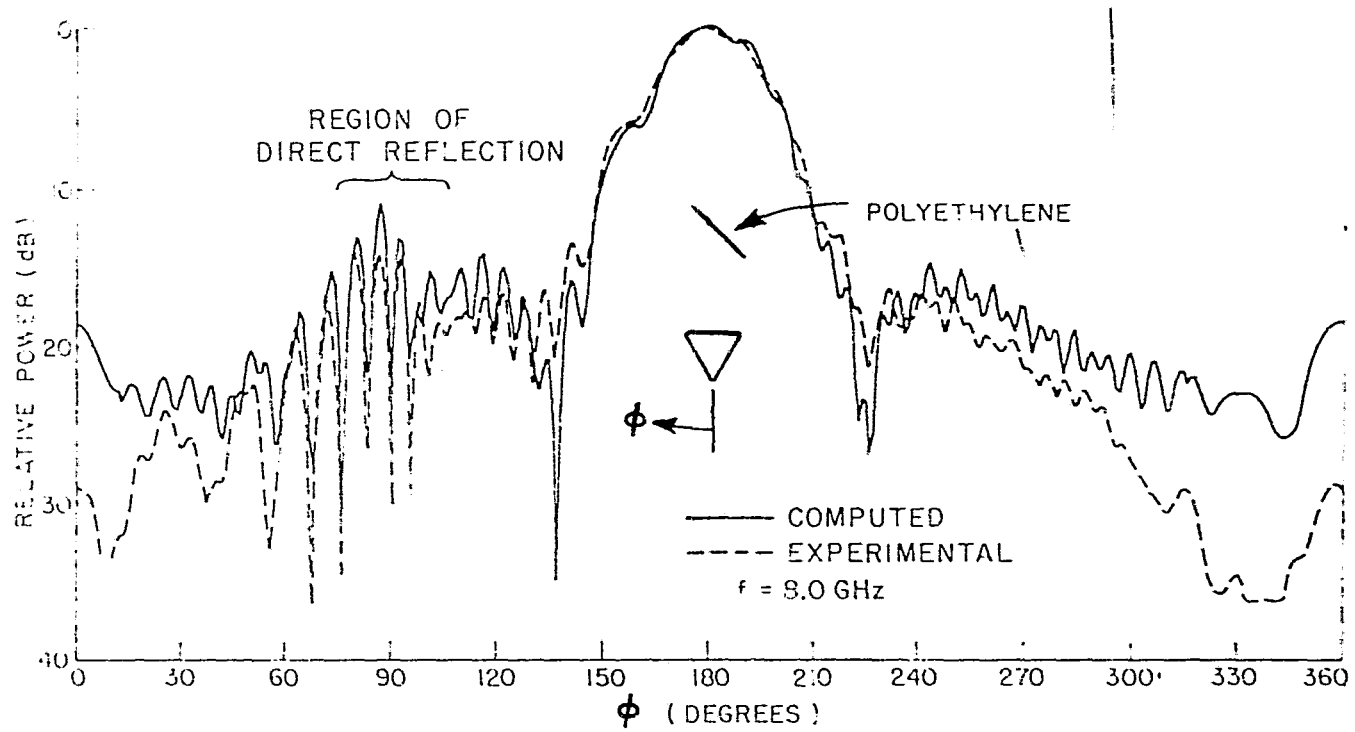


Figure 20. Pattern for scattering from polyethylene strip of thickness .1285" at 8.0 GHz.

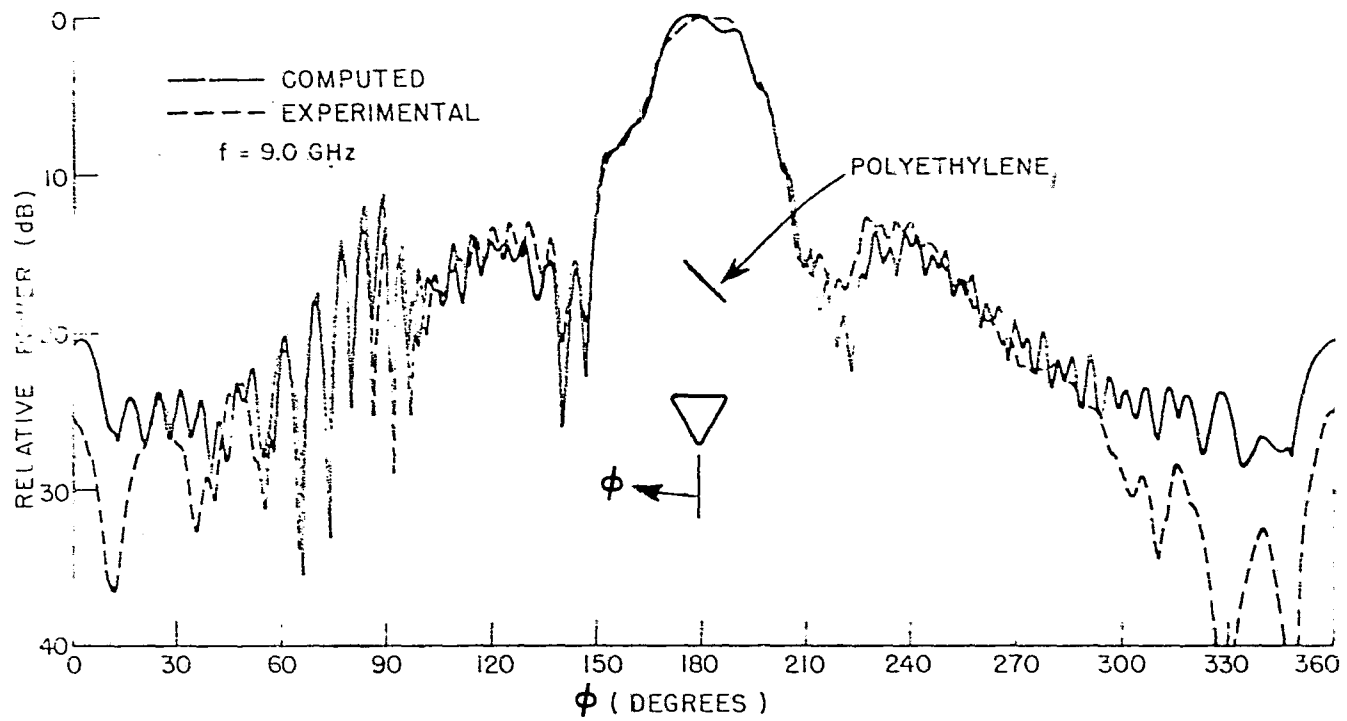


Figure 21. Pattern for scattering from polyethylene strip at 9.0 GHz.

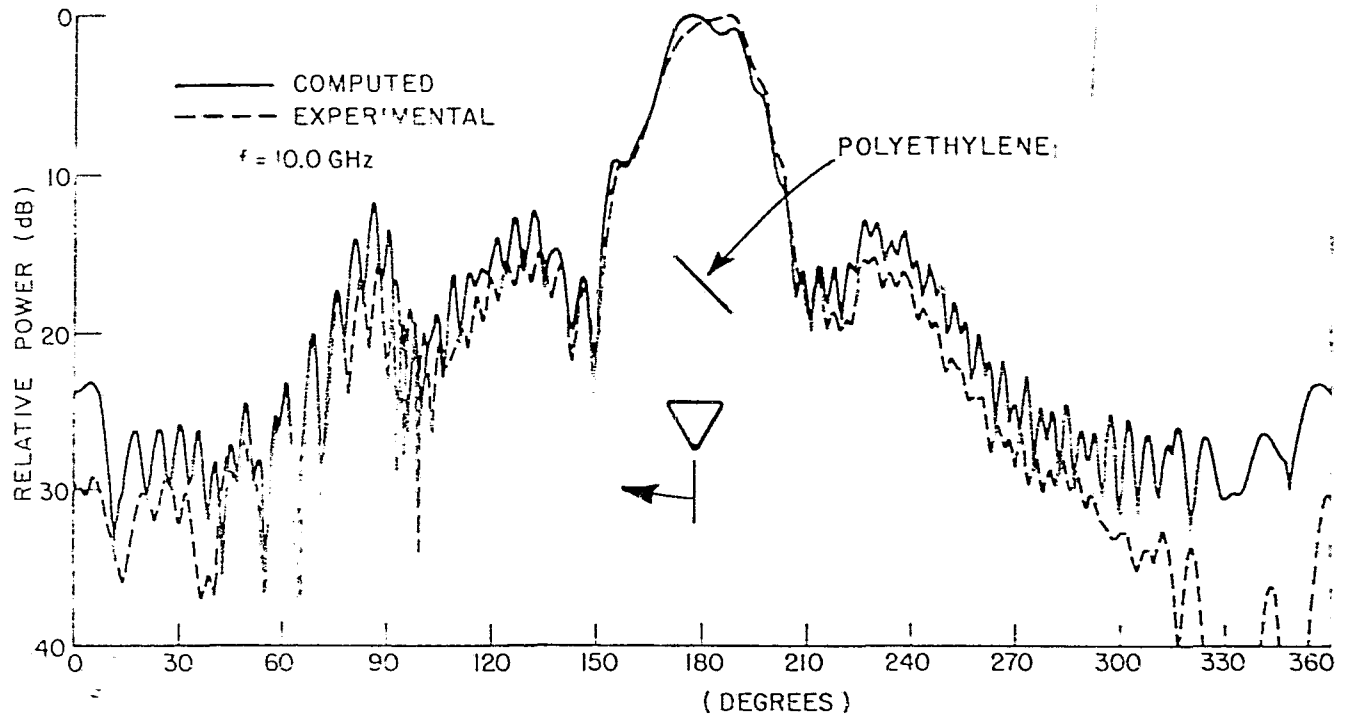


Figure 22. Pattern for scattering from polyethylene strip at 10.0 GHz.

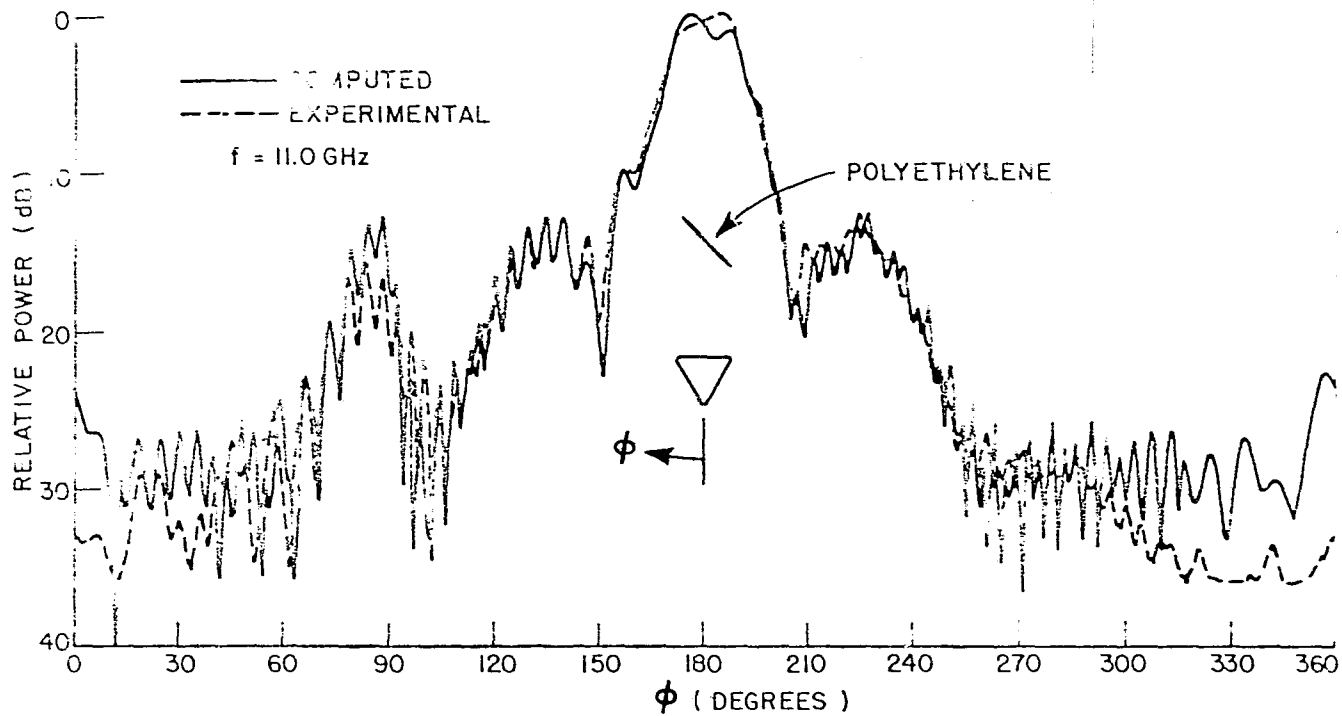


Figure 23. Pattern for scattering from polyethylene strip at 11.0 GHz.

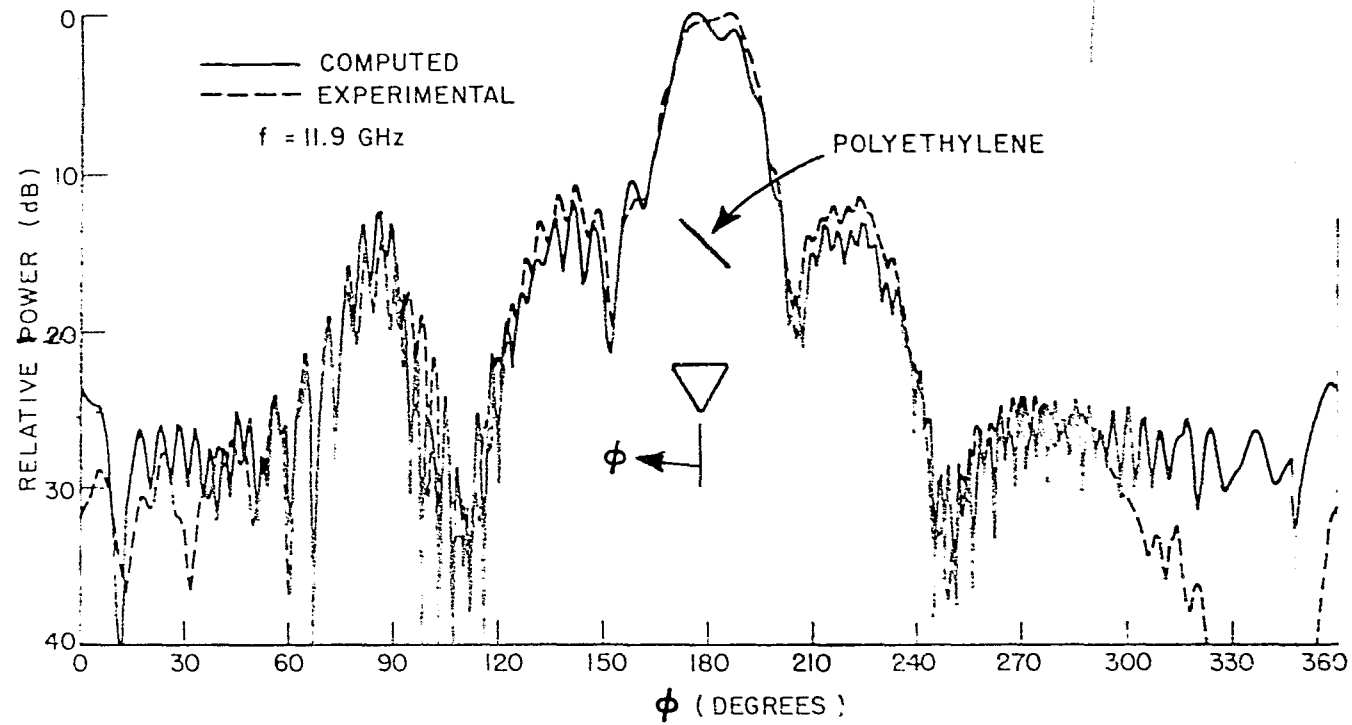


Figure 24. Pattern for scattering from polyethylene strip at 11.9 GHz.

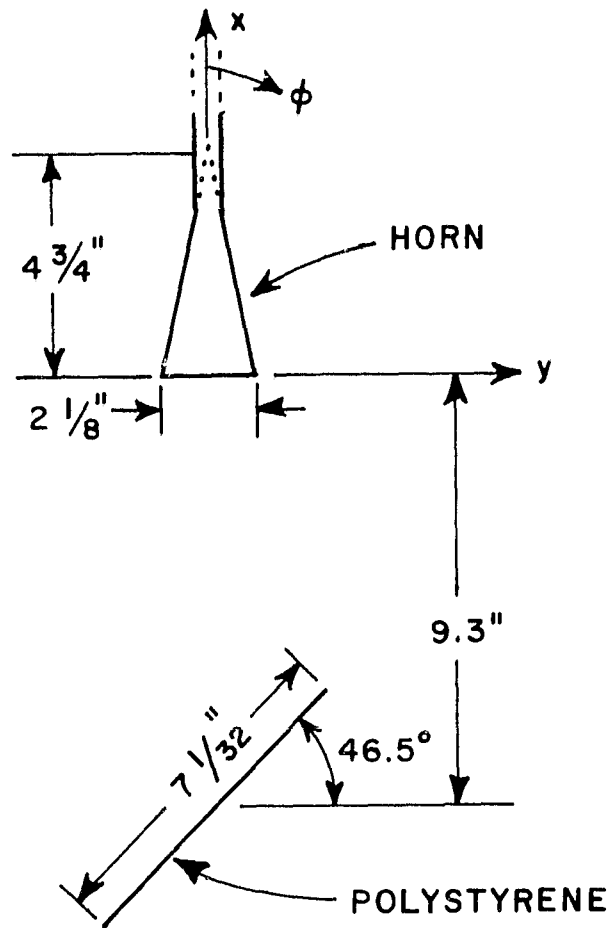


Figure 25. First polystyrene geometry. Slab thickness is .2715" and $\epsilon_r = 2.55$. Measurements taken in the E plane of the horn. Results shown in Figures 26-28. A standard gain horn manufactured by Narda Corp. is used.

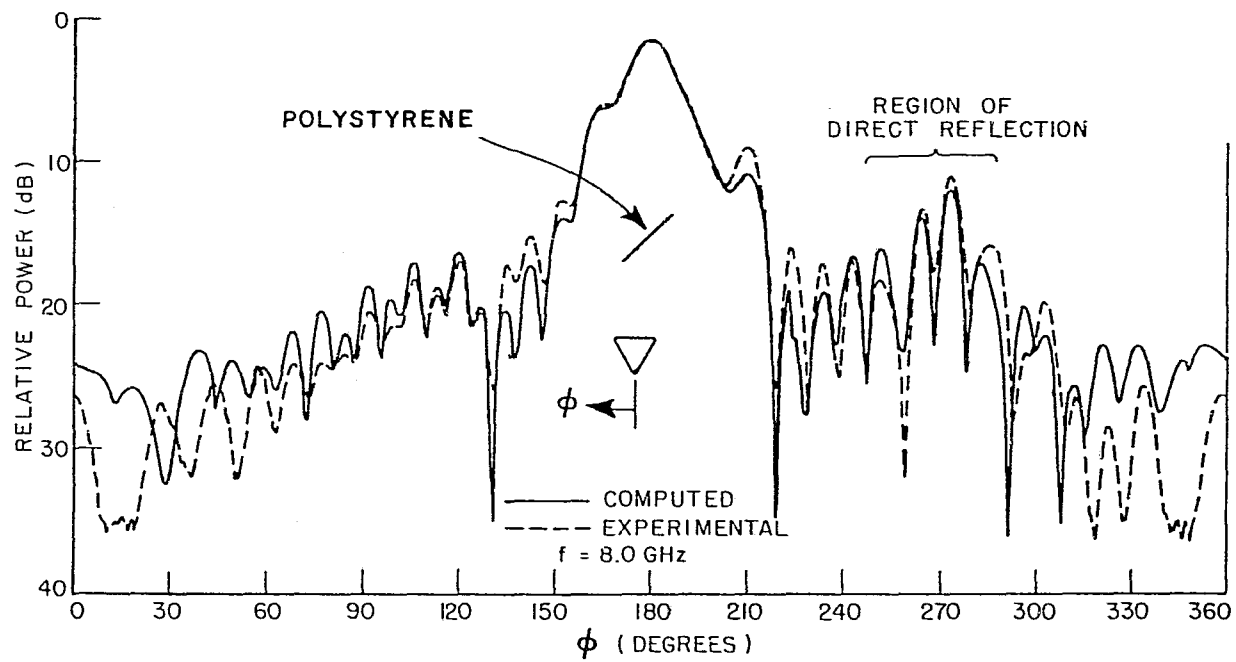


Figure 26. Pattern for polystyrene geometry shown in Figure 25 at 8. GHz.

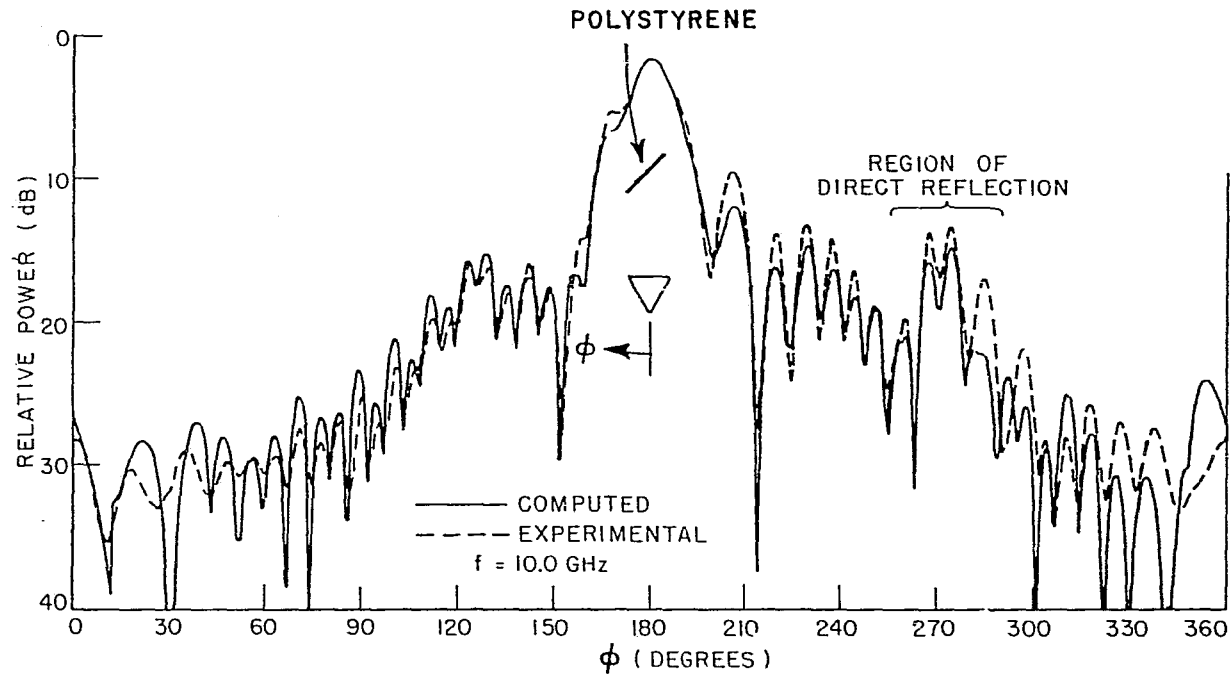


Figure 27. Pattern for polystyrene geometry shown in Figure 25 at 10. GHz.

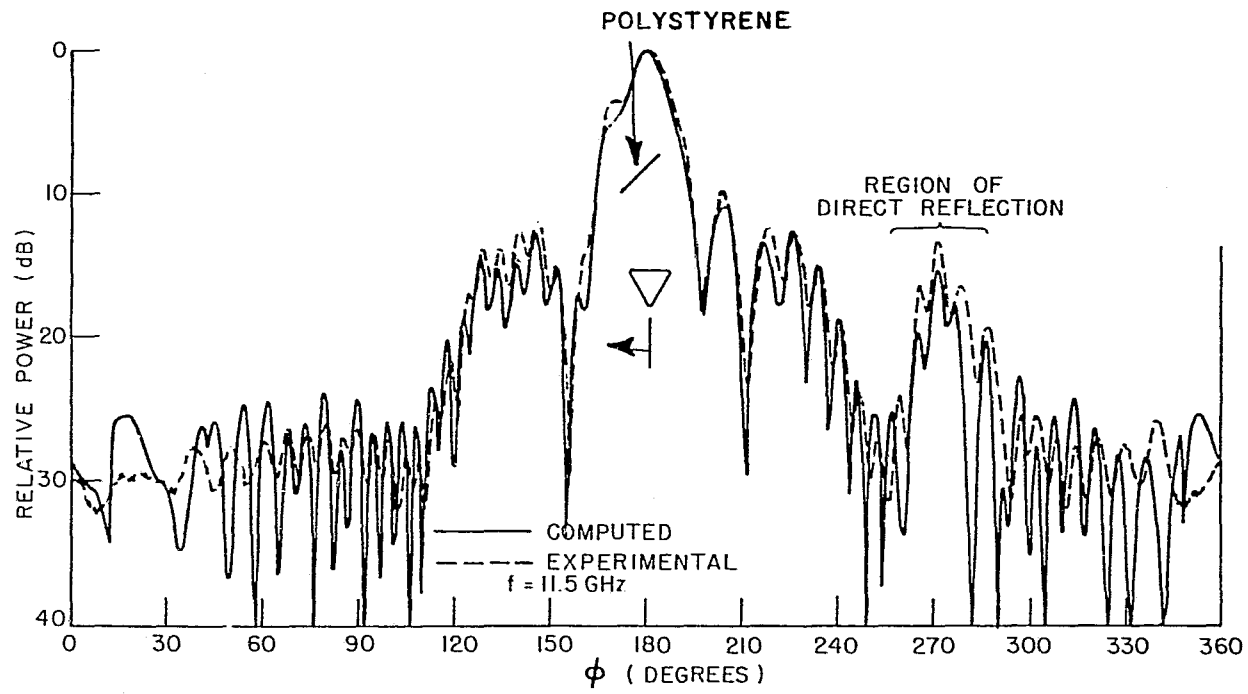


Figure 28. Pattern for polystyrene geometry shown in Figure 25 at 11.5 GHz.

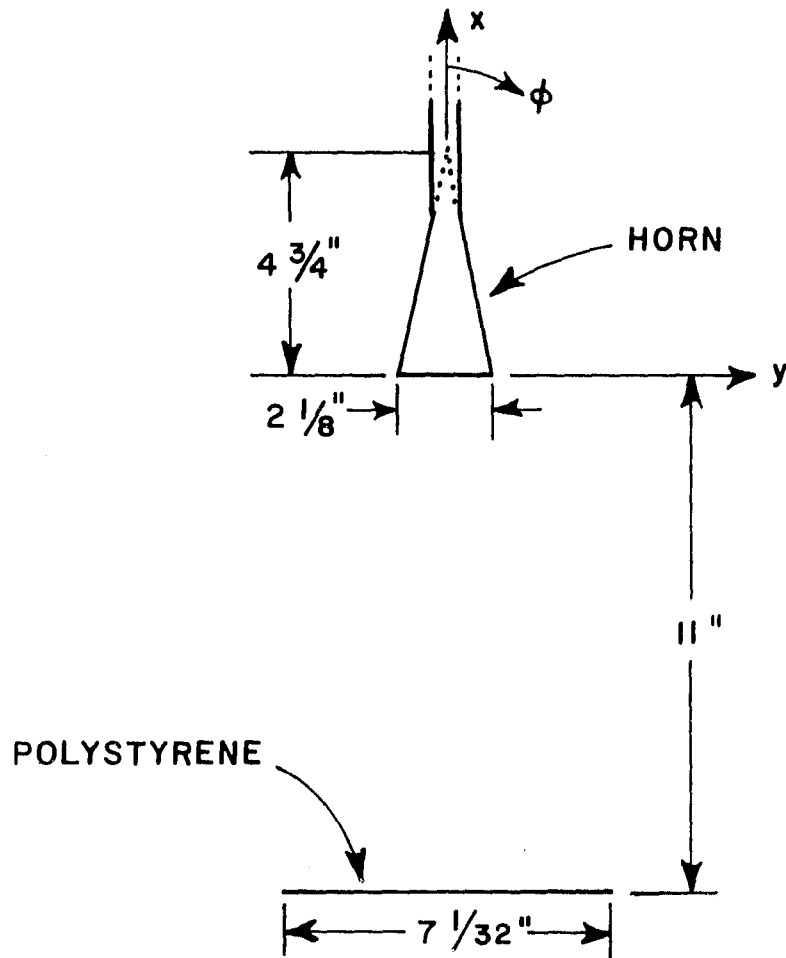


Figure 29. Second polystyrene geometry used especially for investigation of transmission. Again slab thickness is $.2715$ " and $\epsilon_p = 2.55$ with measurements taken in the E plane of the horn. Results shown in Figures 30-34. A standard gain horn manufactured by Narda Corp. is used.

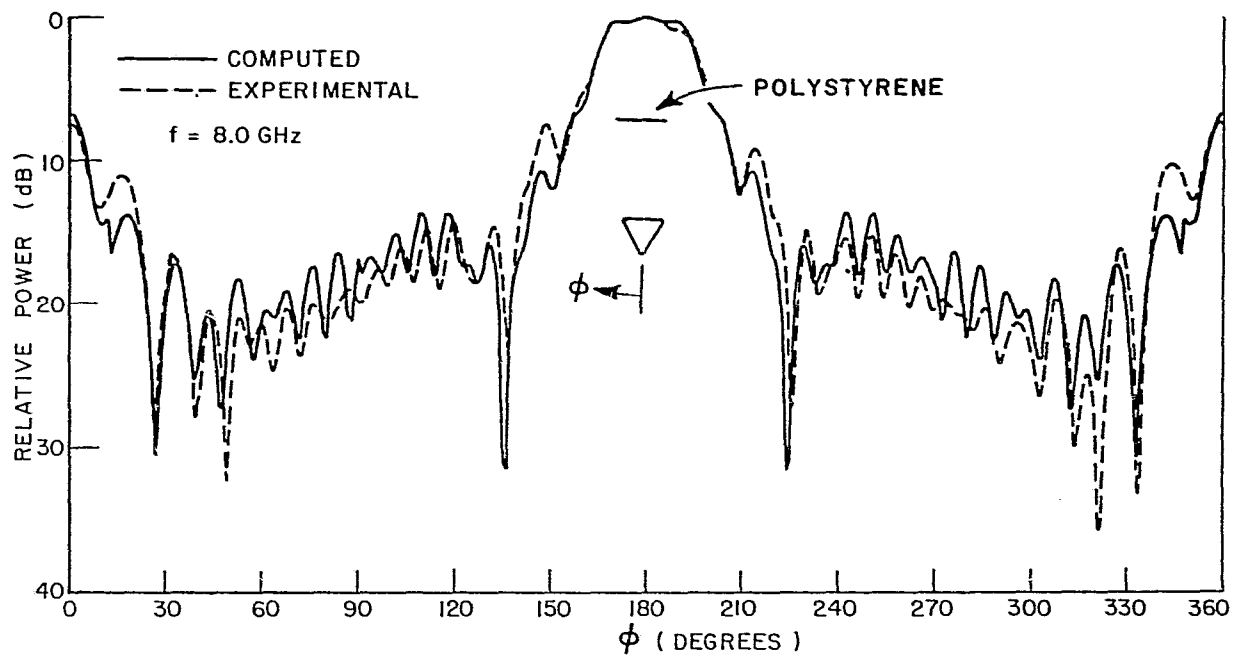


Figure 30. Pattern for polystyrene geometry shown in Figure 29 at 8. GHz.

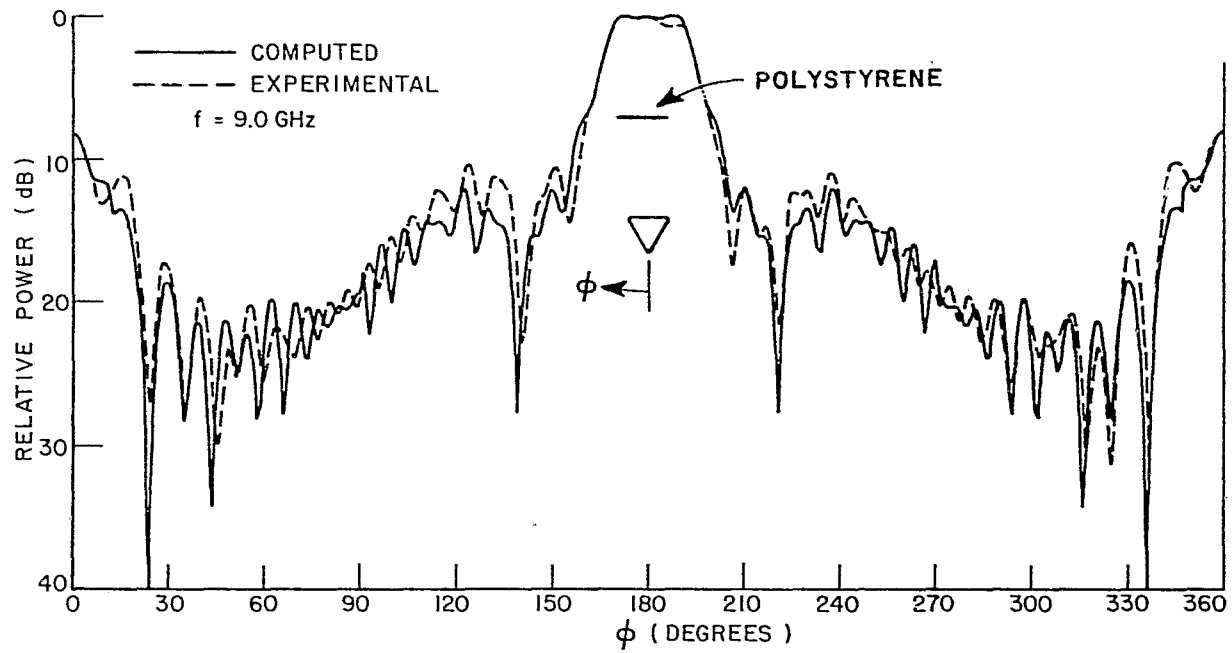


Figure 31. Pattern for polystyrene geometry shown in Figure 29 at 9. GHz.

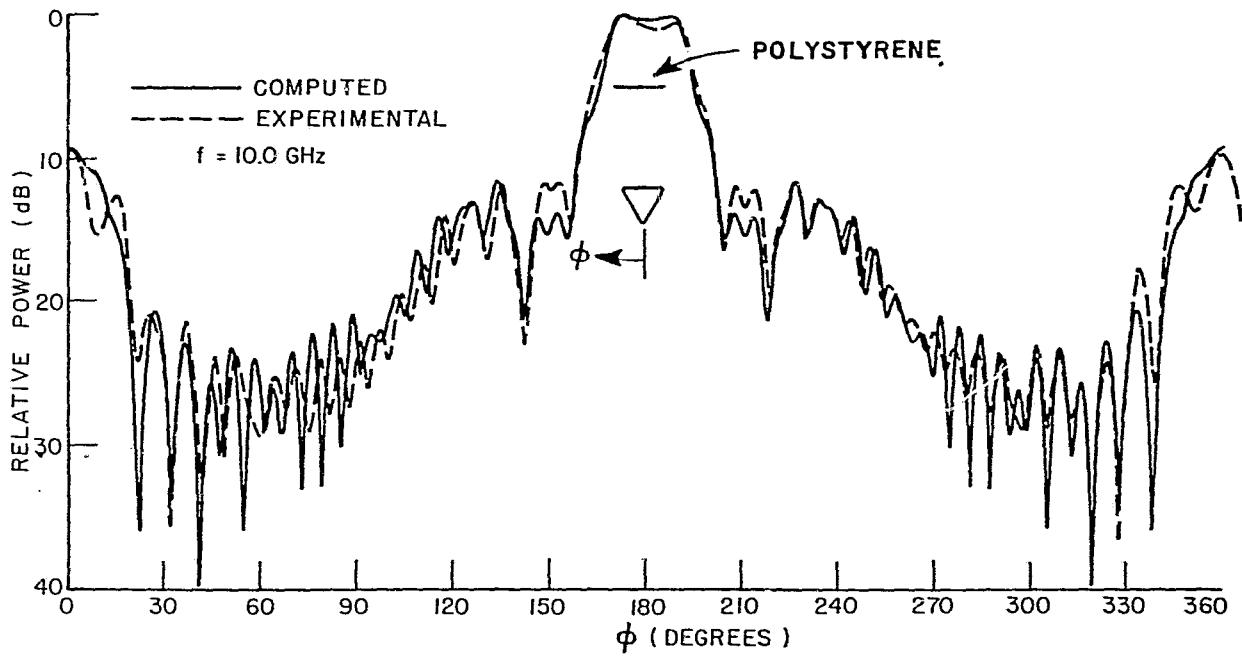


Figure 32. Pattern for polyethylene geometry shown in Figure 29 at 10. GHz.

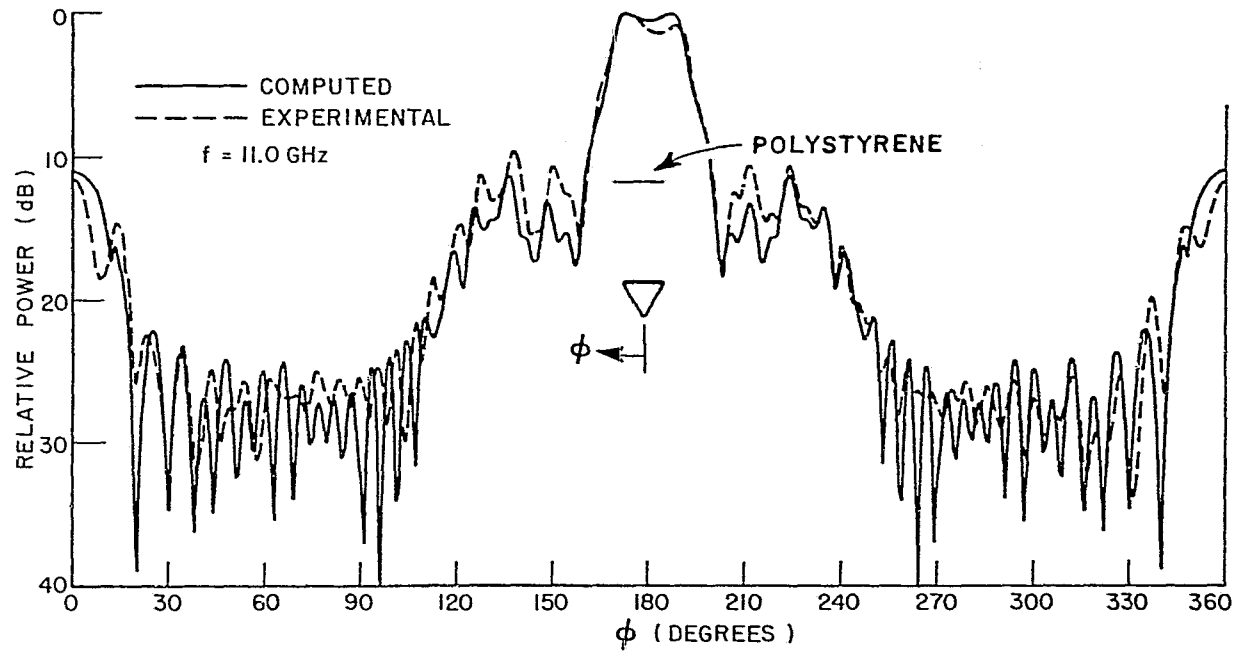


Figure 33. Pattern for polyethylene geometry shown in Figure 29 at 11. GHz.

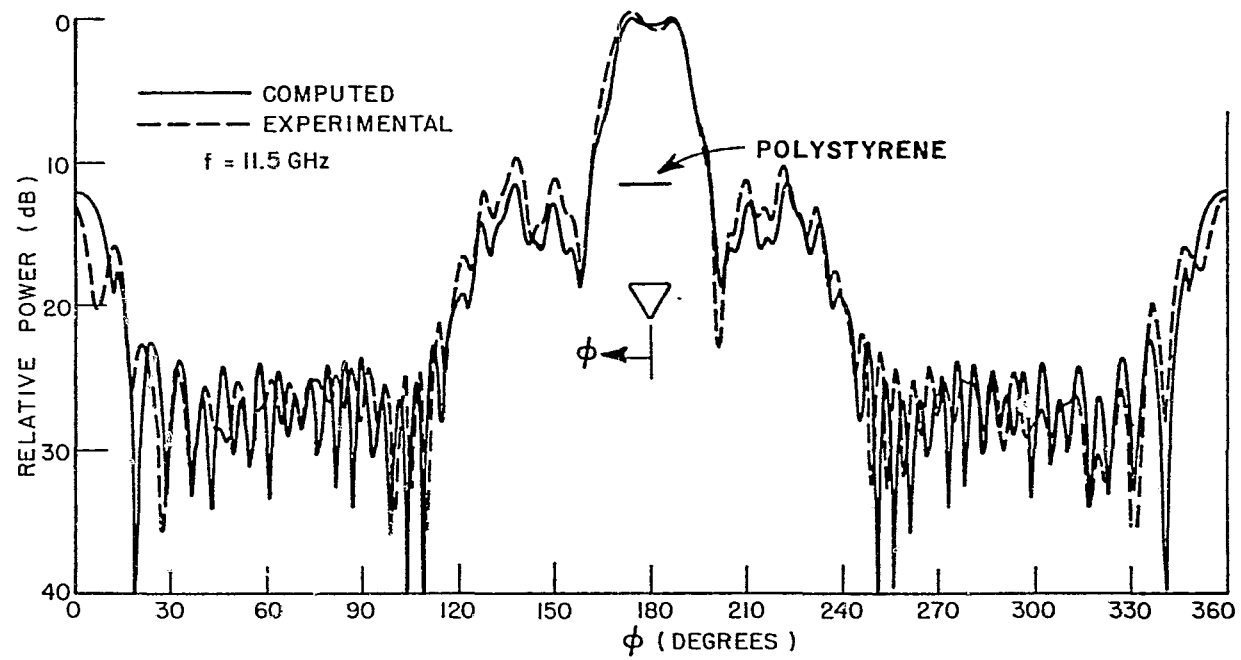


Figure 34. Pattern for polyethylene geometry shown in Figure 29 at 11.5 GHz.

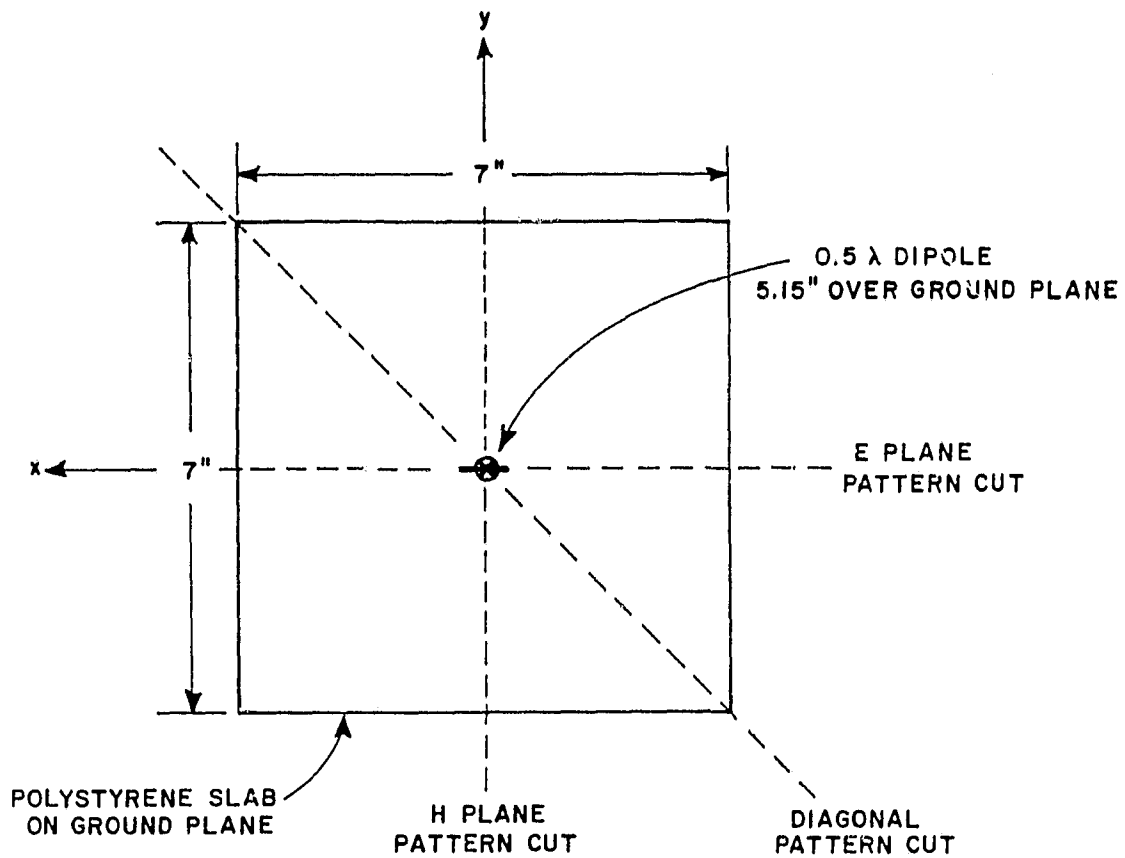


Figure 35. A polystyrene slab which is .2715" thick and $\epsilon = 2.55$ is mounted flush on a square ground plane. The structure is illuminated by a dipole mounted 5.15" above the center of the plate. Using normal spherical coordinates, the patterns are measured by varying θ with ϕ a constant. Note that the z axis is into the page.

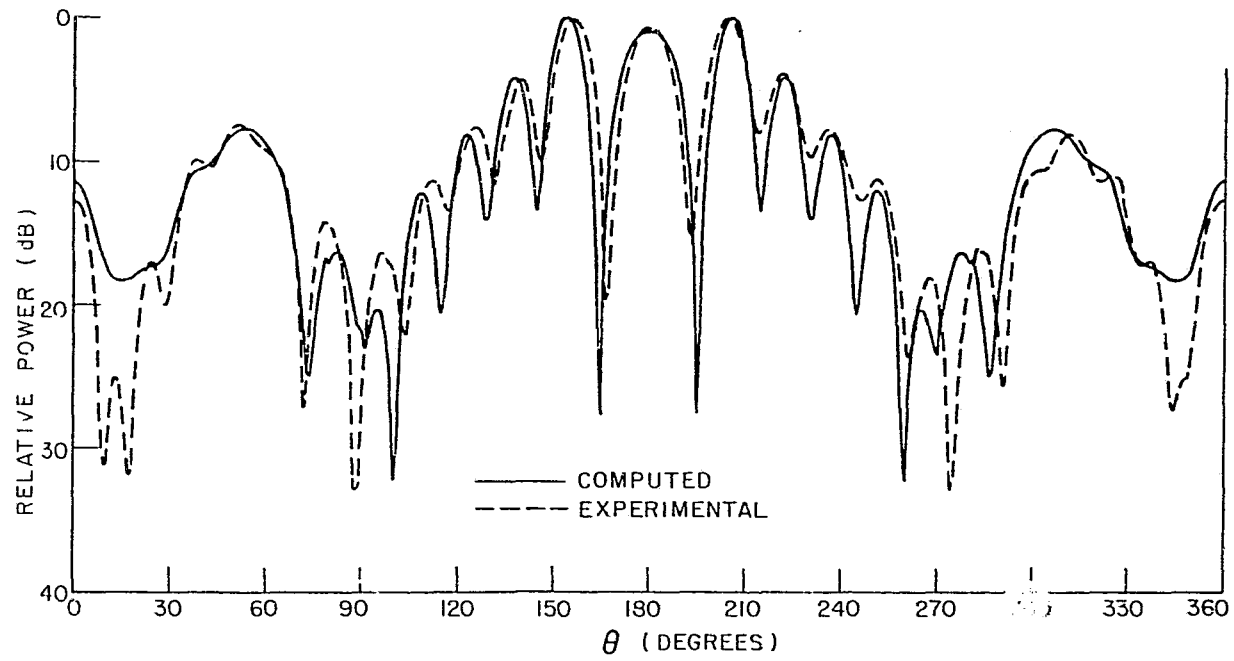


Figure 36. E plane pattern for geometry illustrated in Figure 35.

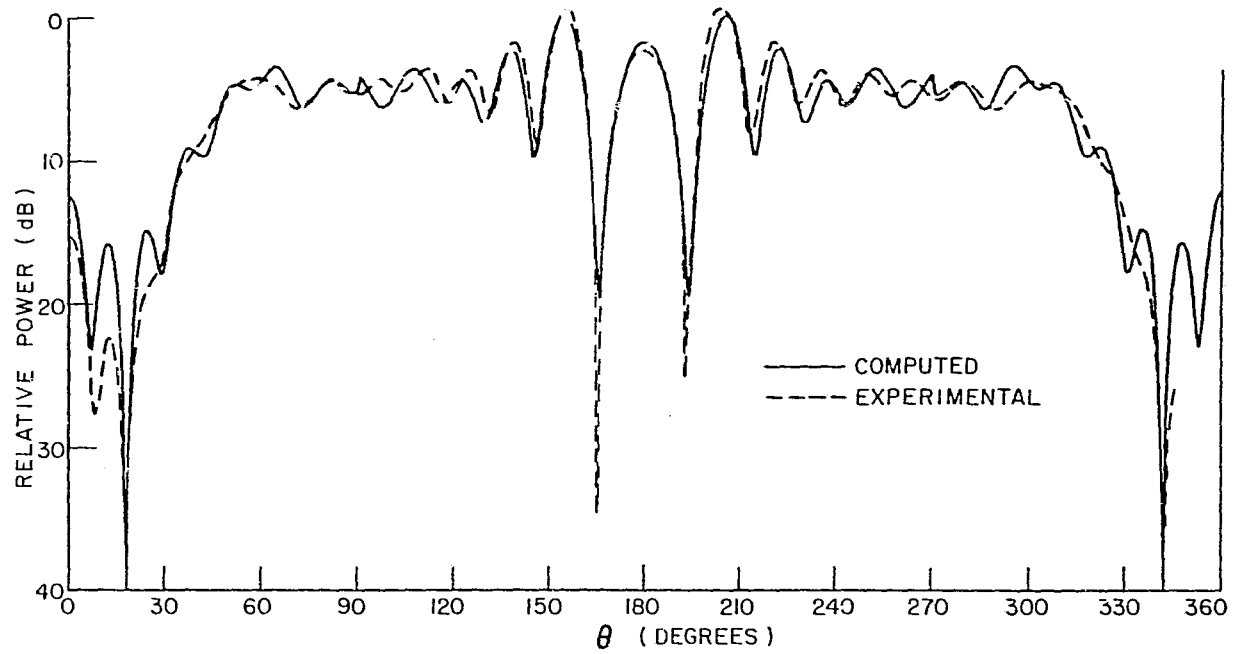


Figure 37. H plane pattern for geometry illustrated in Figure 35.

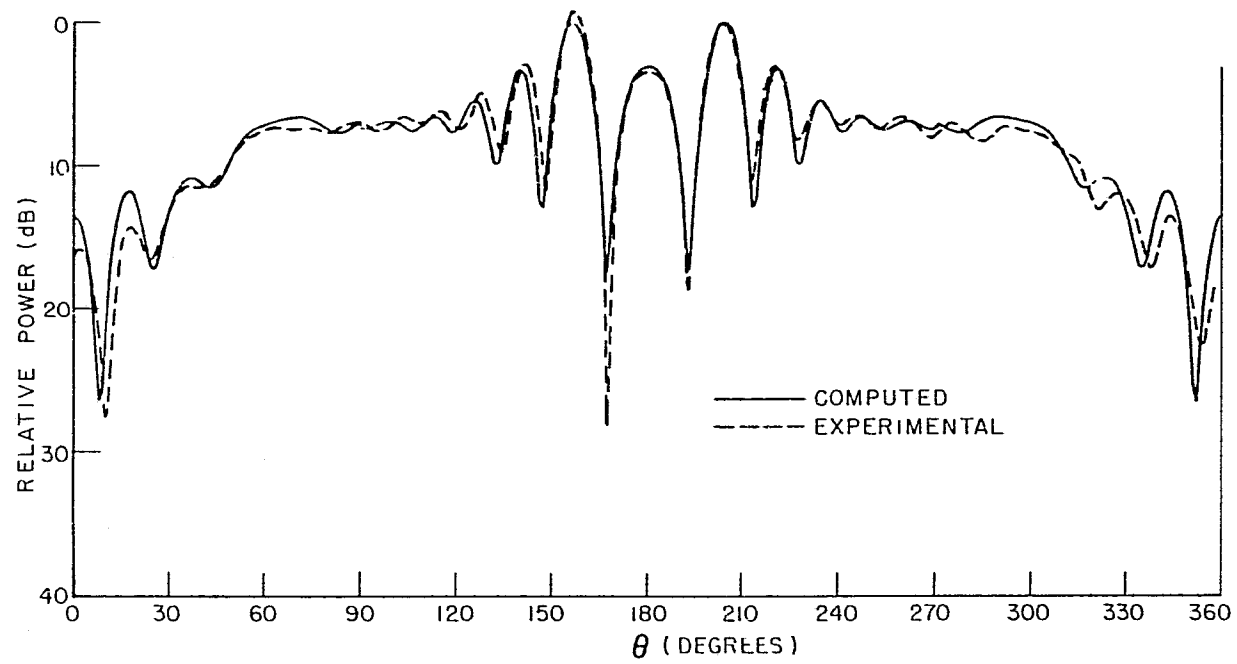


Figure 38. θ component of diagonal pattern for geometry illustrated in Figure 35.
(Receiving horn in H plane)

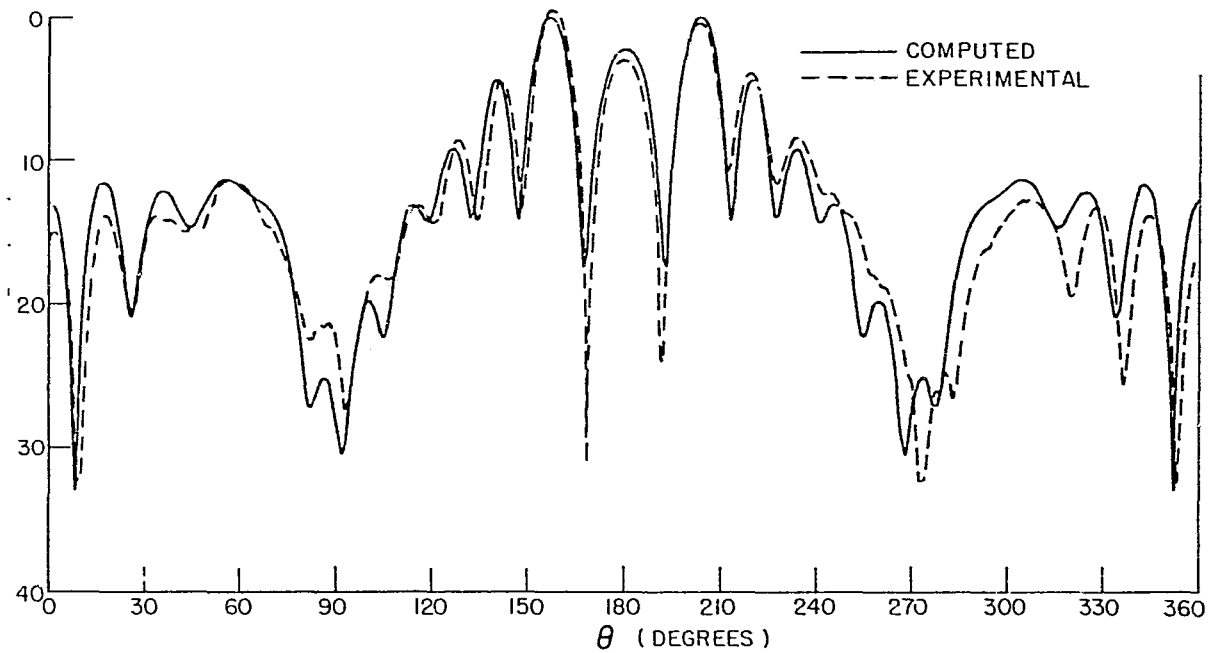


Figure 39. ϕ component of diagonal pattern for geometry illustrated in Figure 35. ('Receiving horn in E plane').

In order to illustrate the effect of the dielectric layer, a comparison is made between these patterns and corresponding patterns obtained from the same geometry in which the dielectric layer is removed in Figures 40-43. It is apparent that the dielectric does significantly affect the pattern making this geometry a valid test of the dielectric theory.

D. Comparison with Moment Method

Further confirmation is obtained, as well as a study of applicability by comparison of results of this theory with Moment Method results [10,11] using the geometry shown in Figure 44. The moment method results, as presented here, are assumed to be the exact solutions to these problems. Working with first an electric and then a magnetic line source, the effects of varying source to strip distance and angle of incidence are studied. Results for varying the source range are shown in Figures 45 and 46. Here it is noted that our results are accurate at ranges of greater than a wavelength, but begin to break down inside that range. Results for varying the angle of incidence are shown in Figures 47 and 48. It is apparent here that the solutions are accurate to at least 40° off normal incidence and can perhaps be extended to 60° off normal incidence.

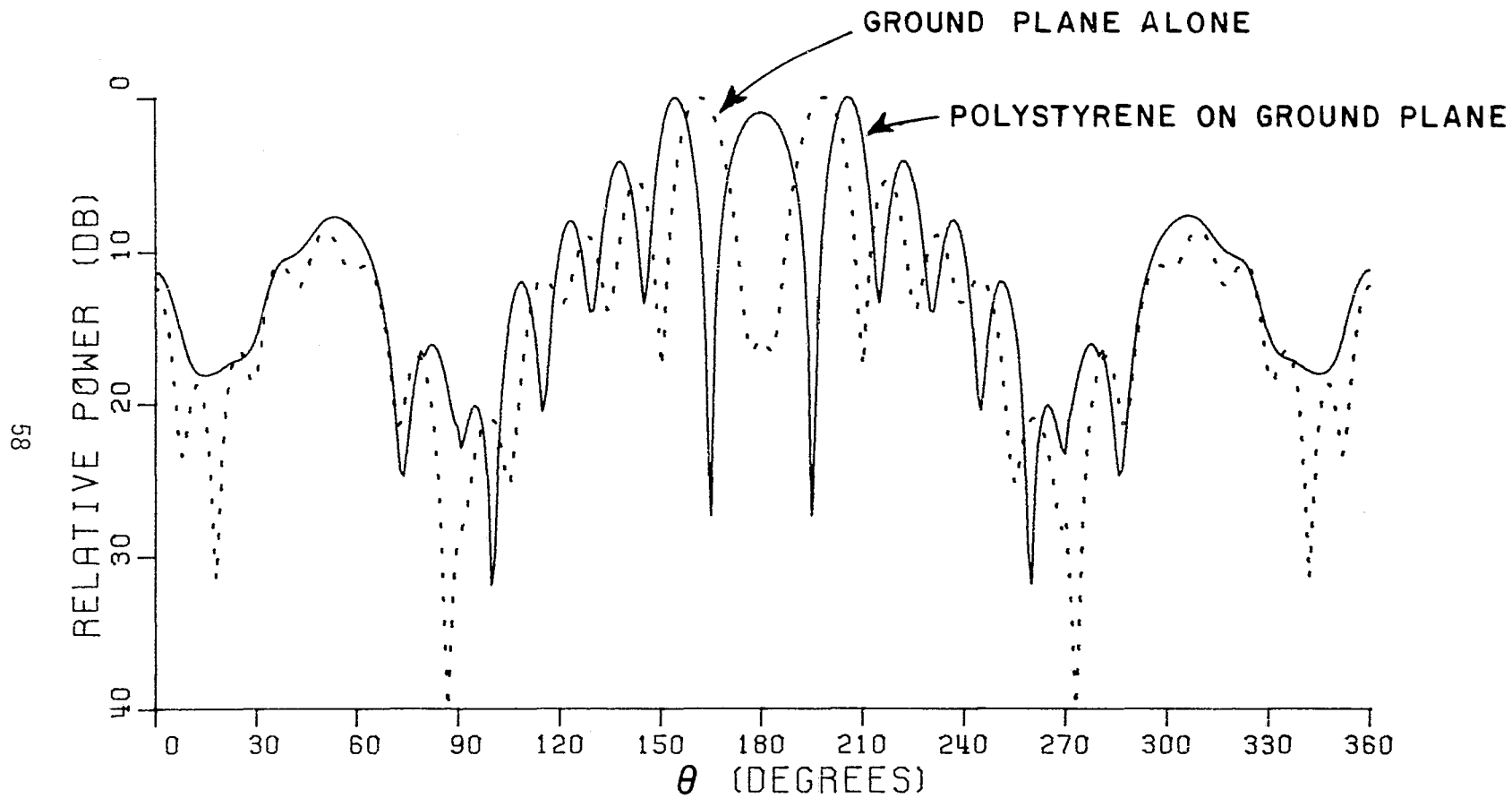


Figure 40. Comparison of E plane patterns of geometry illustrated in Figure 35 with (solid line) and without (dashed line) the polystyrene slab.

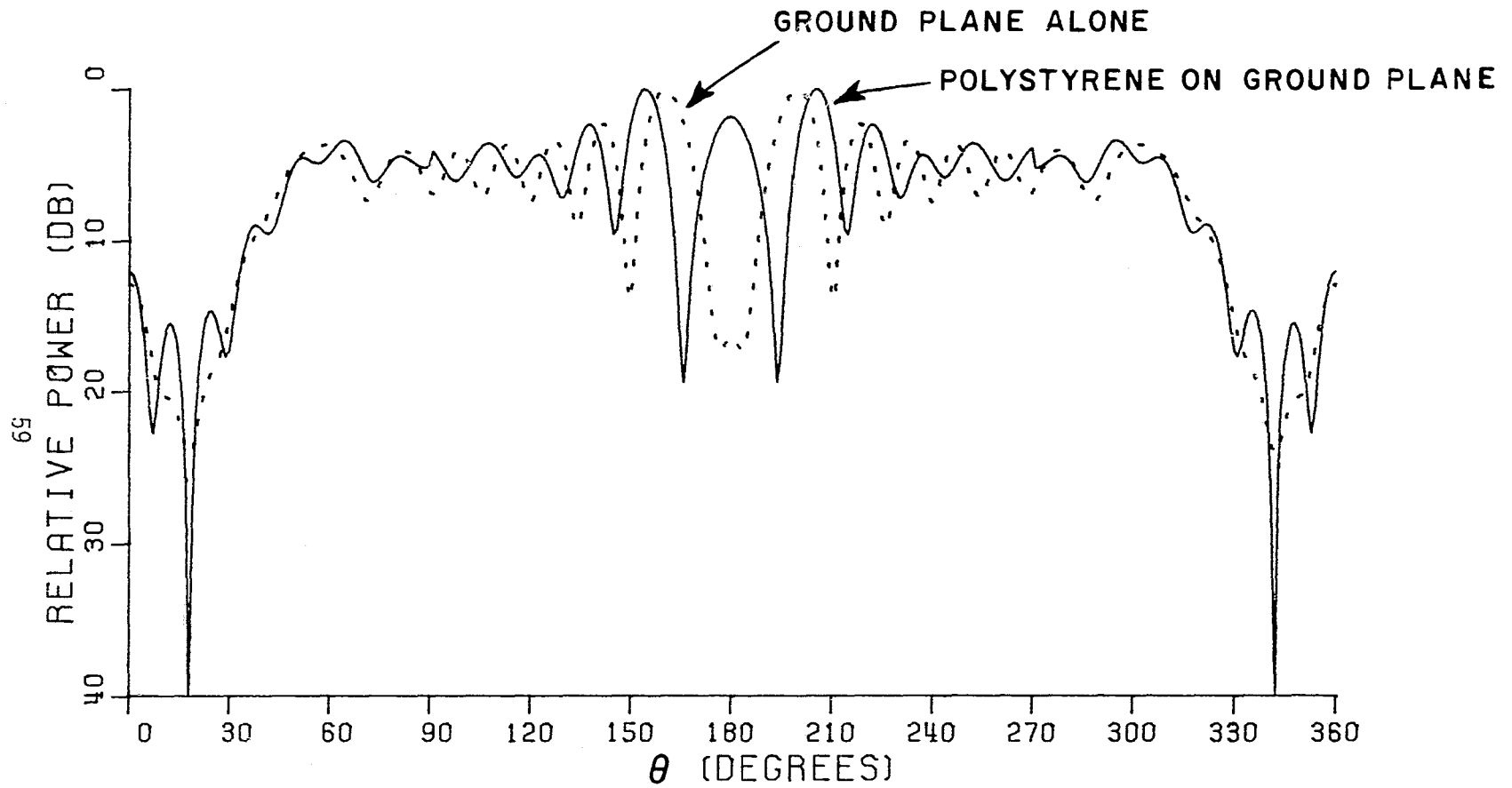


Figure 41. Comparison of H plane patterns of geometry illustrated in Figure 35 with (solid line) and without (dashed line) the polystyrene slab.

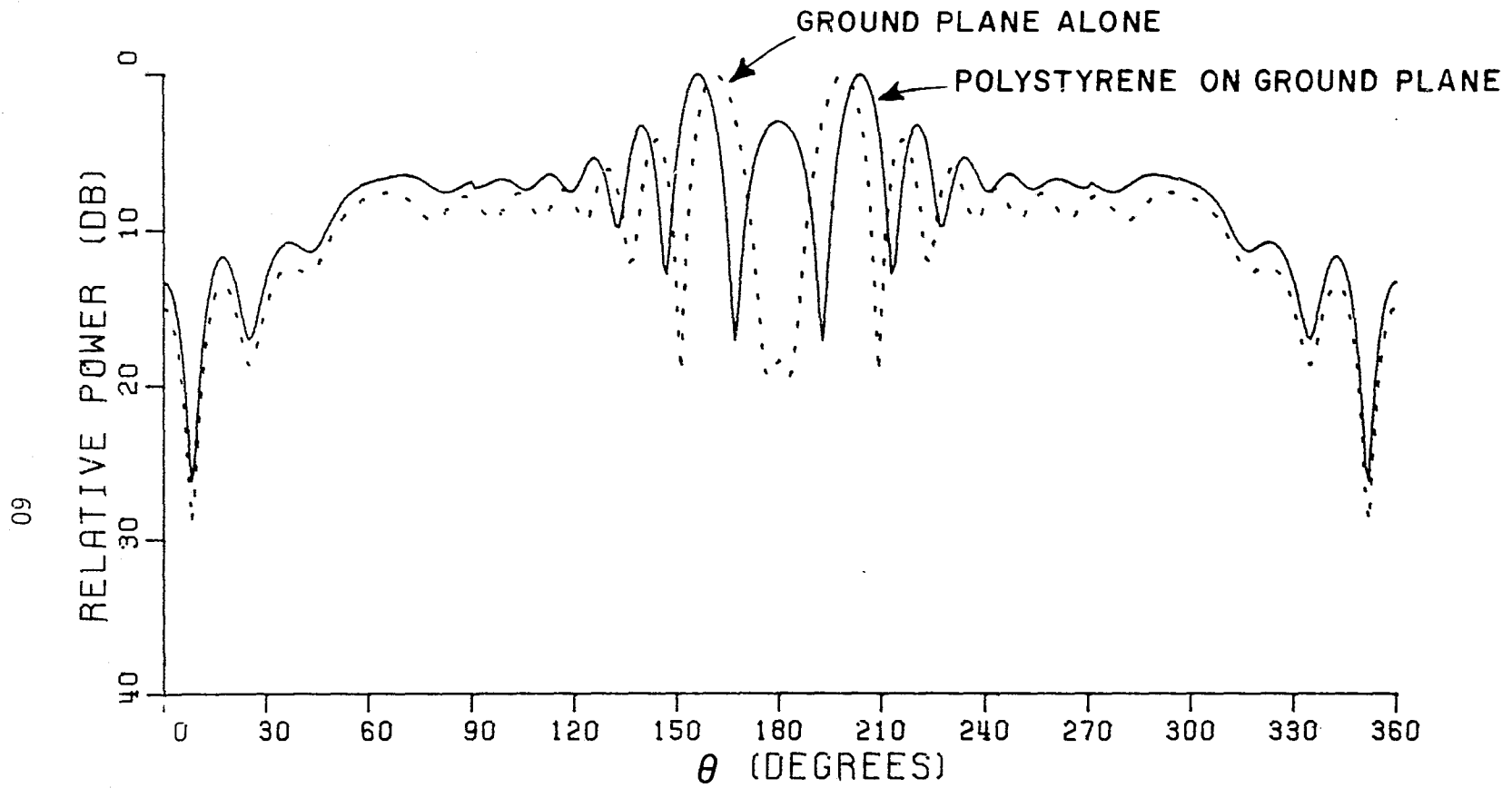


Figure 42. Comparison of θ components of diagonal patterns of geometry illustrated in Figure 35 with (solid line) and without (dashed line) the polystyrene slab. (Receiving horn in H plane.)

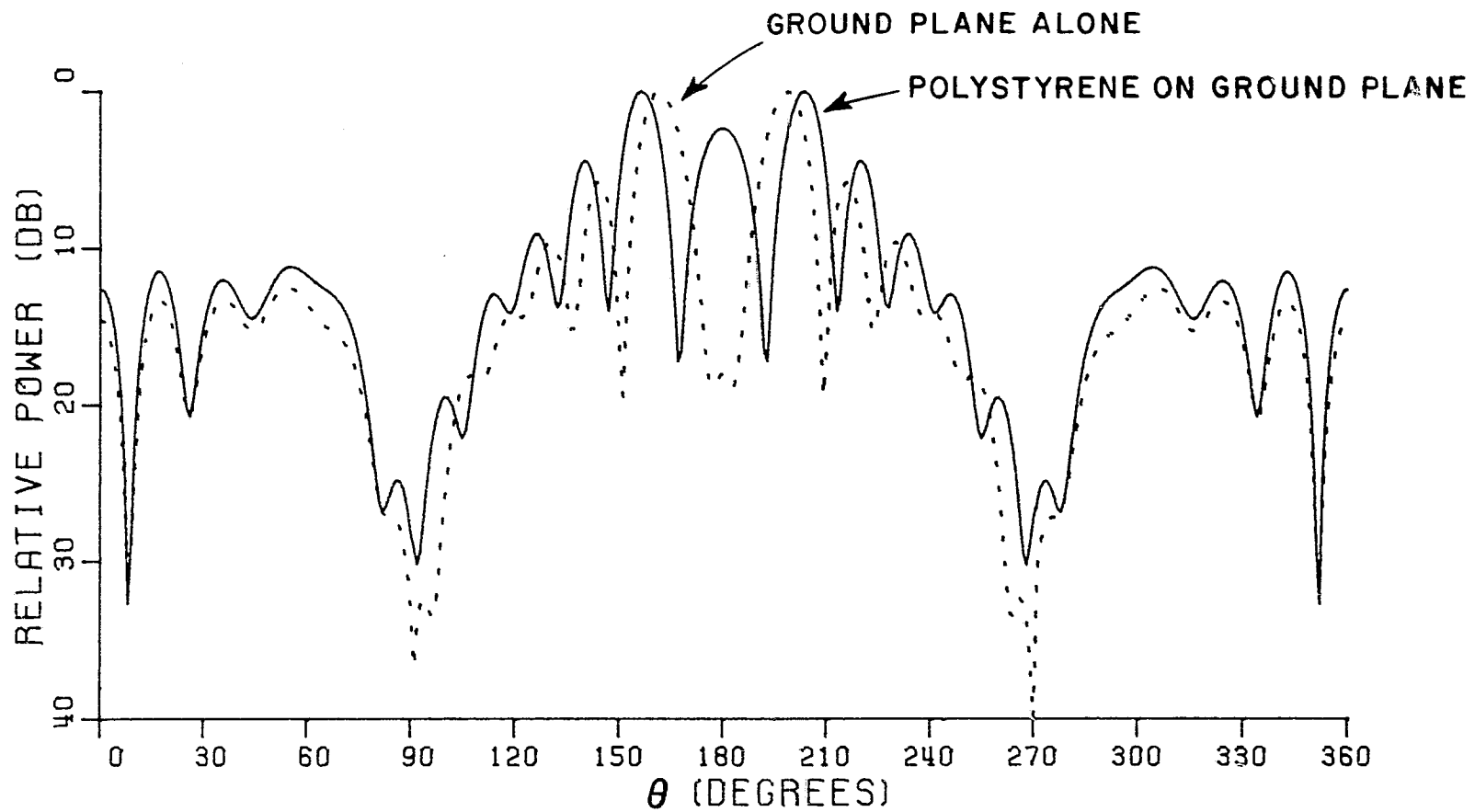


Figure 43. Comparison of ϕ components of diagonal patterns of geometry illustrated in Figure 35 with (solid line) and without (dashed line) the polystyrene slab. (Receiving horn in E plane.)

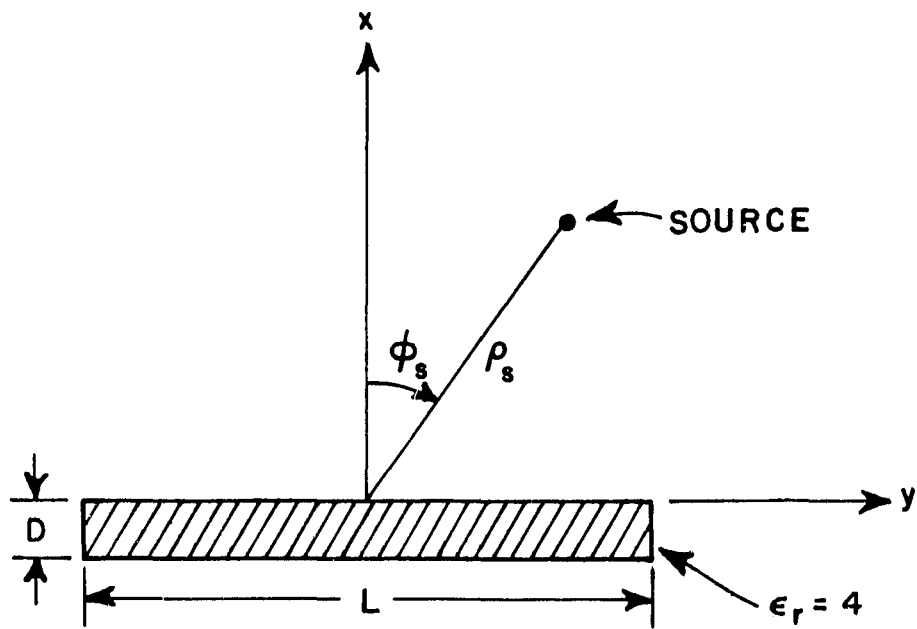


Figure 44. Geometry used for GTD-Moment Method comparison. Note that ϕ_s and ρ_s are varied for an electric and a magnetic line source.

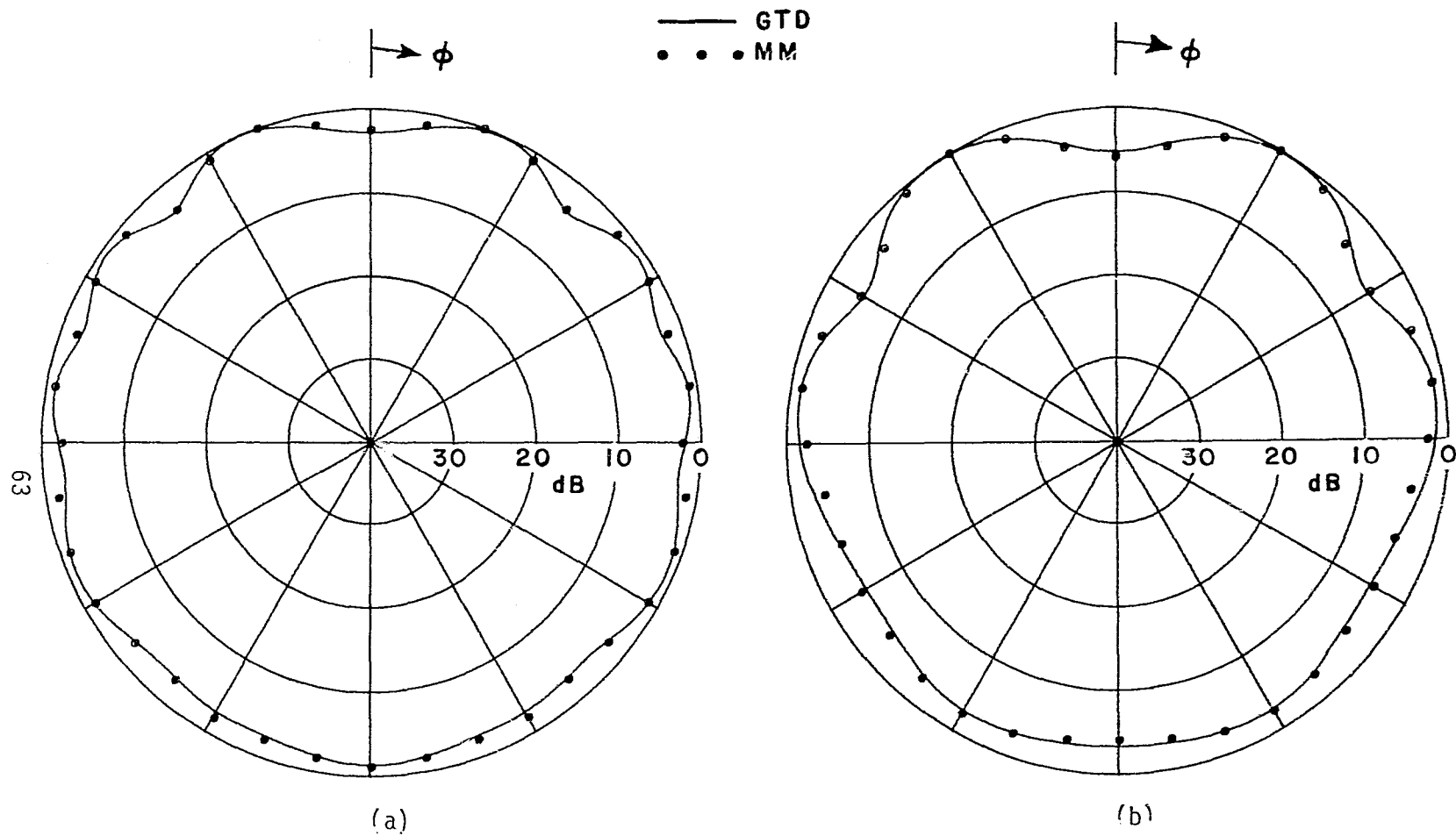


Figure 45. GTD-MM comparison with electric line source and varying ρ_s , using geometry shown in Figure 44 with $L=2.0\lambda$, $D=.05\lambda$, $\phi_s=0$. (a) $\rho_s=2.0\lambda$. (b) $\rho_s=1.0\lambda$.

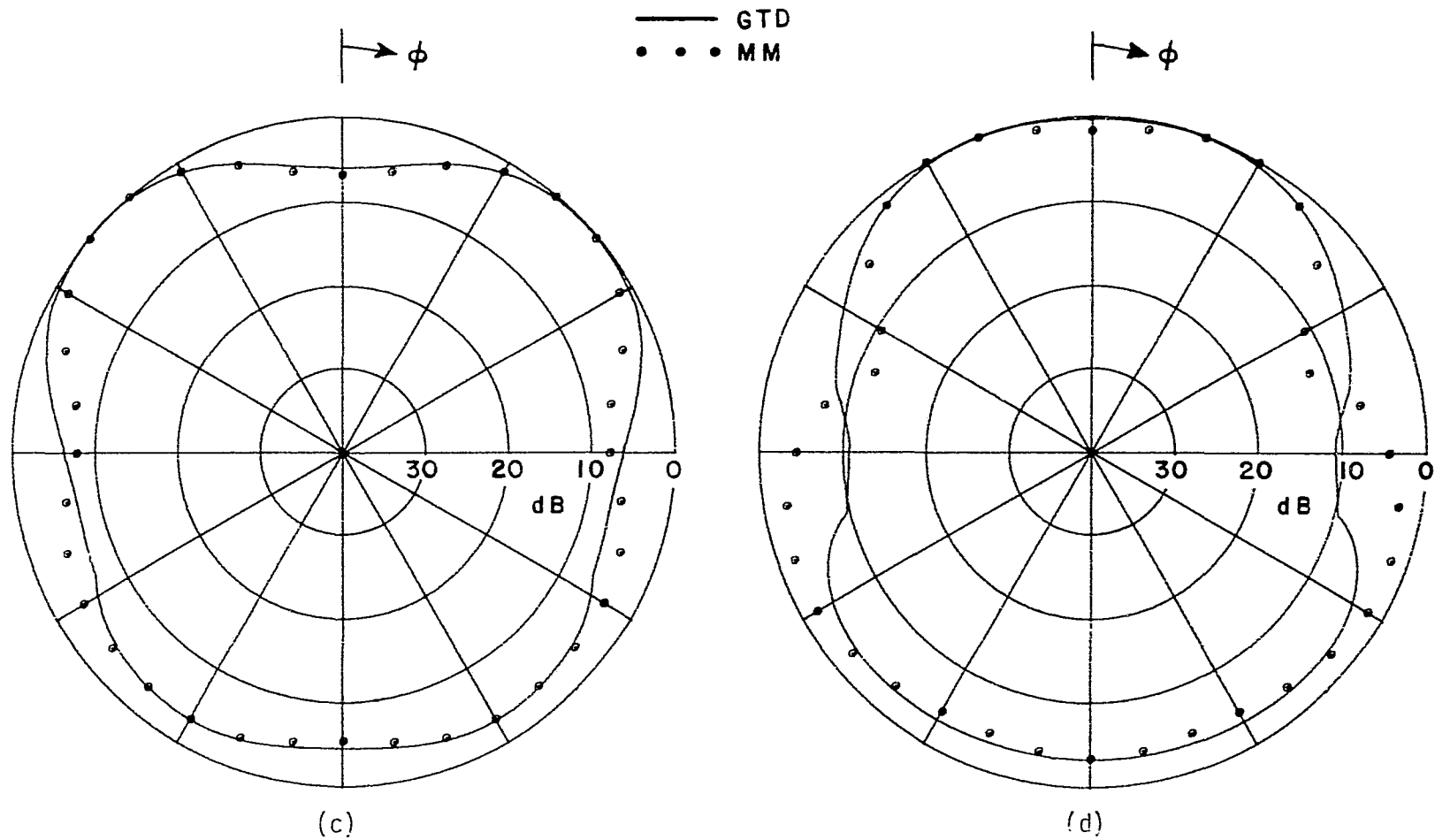


Figure 45. GTD-MM comparison with electric line source and varying ρ_S , using geometry shown in Figure 44 with $L=2\lambda$, $D=.05\lambda$, $\phi_S=0$. (c) $\rho_S=.5\lambda$. (d) $\rho_S=.25\lambda$.

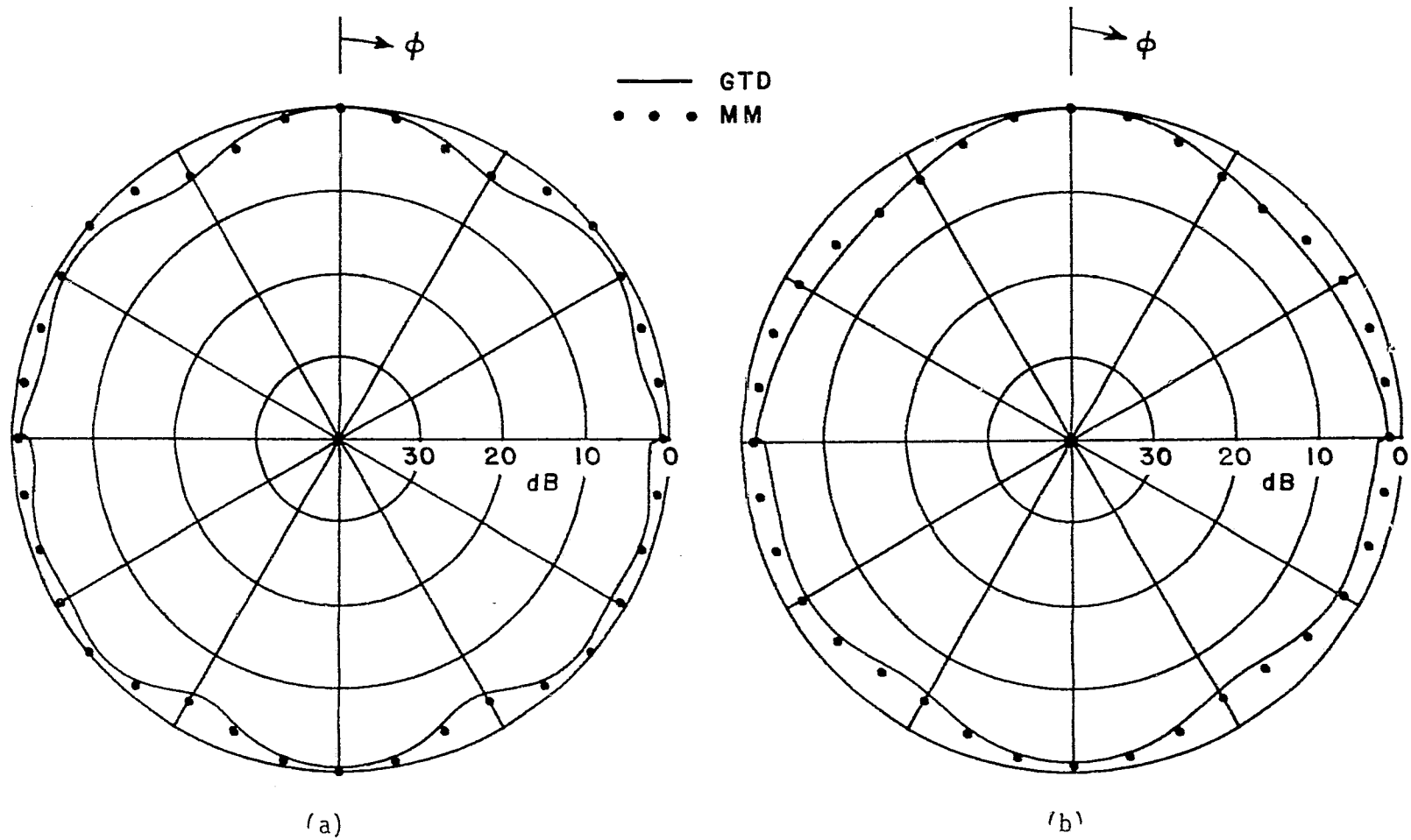


Figure 46. GTD-MM comparison with magnetic line source and varying ρ_S , using geometry shown in Figure 44 with $L=1\lambda$, $D=.1\lambda$, $\phi_S=0$. (a) $\rho_S=2\lambda$. (b) $\rho_S=1\lambda$.

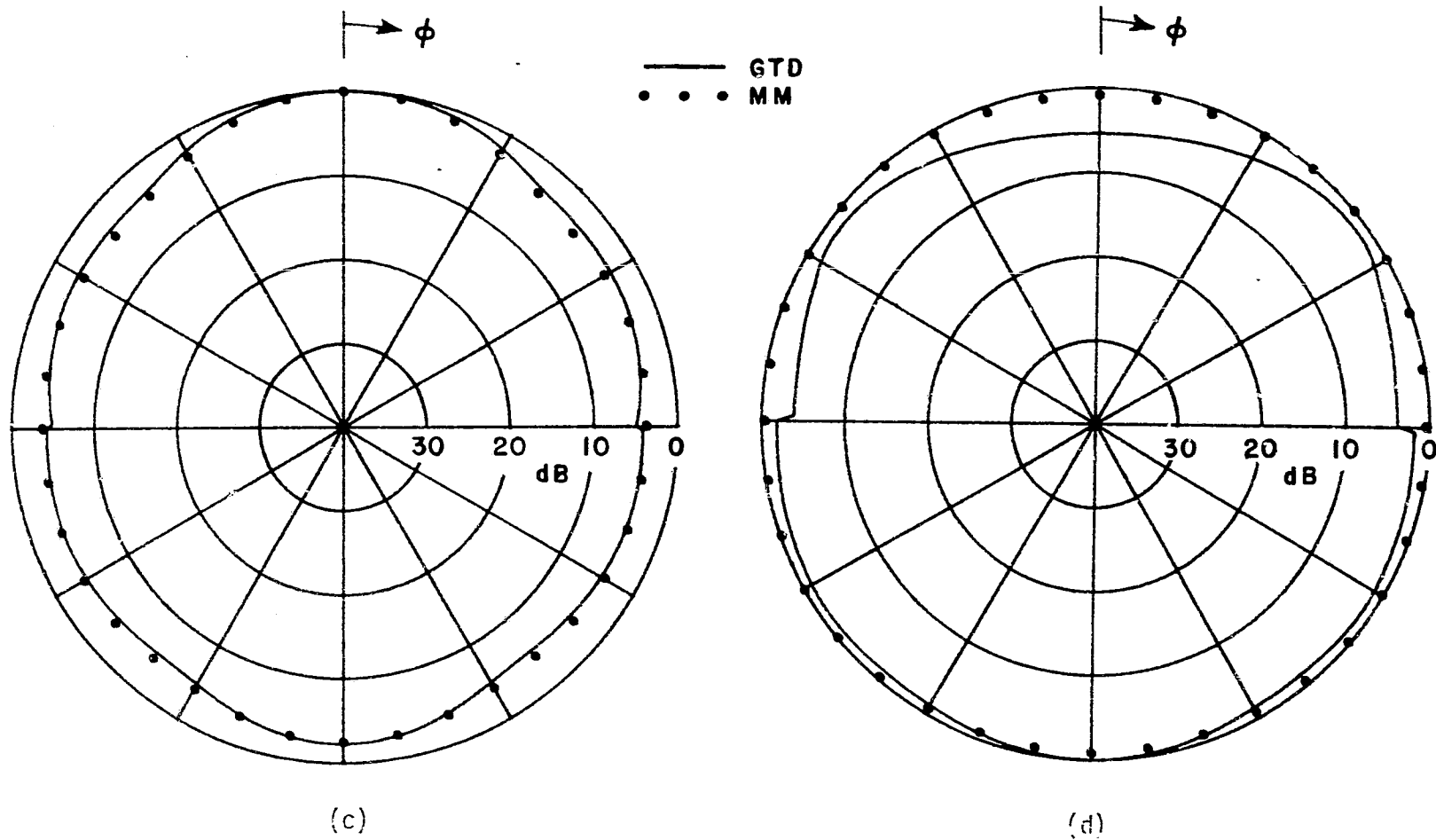


Figure 46. GTD-MM comparison with magnetic line source and varying ρ_s , using geometry shown in Figure 44 with $L=1.1\lambda$, $D=.1\lambda$, $\phi_s=0$. (c) $\rho_s=.5\lambda$. (d) $\rho_s=.25\lambda$.

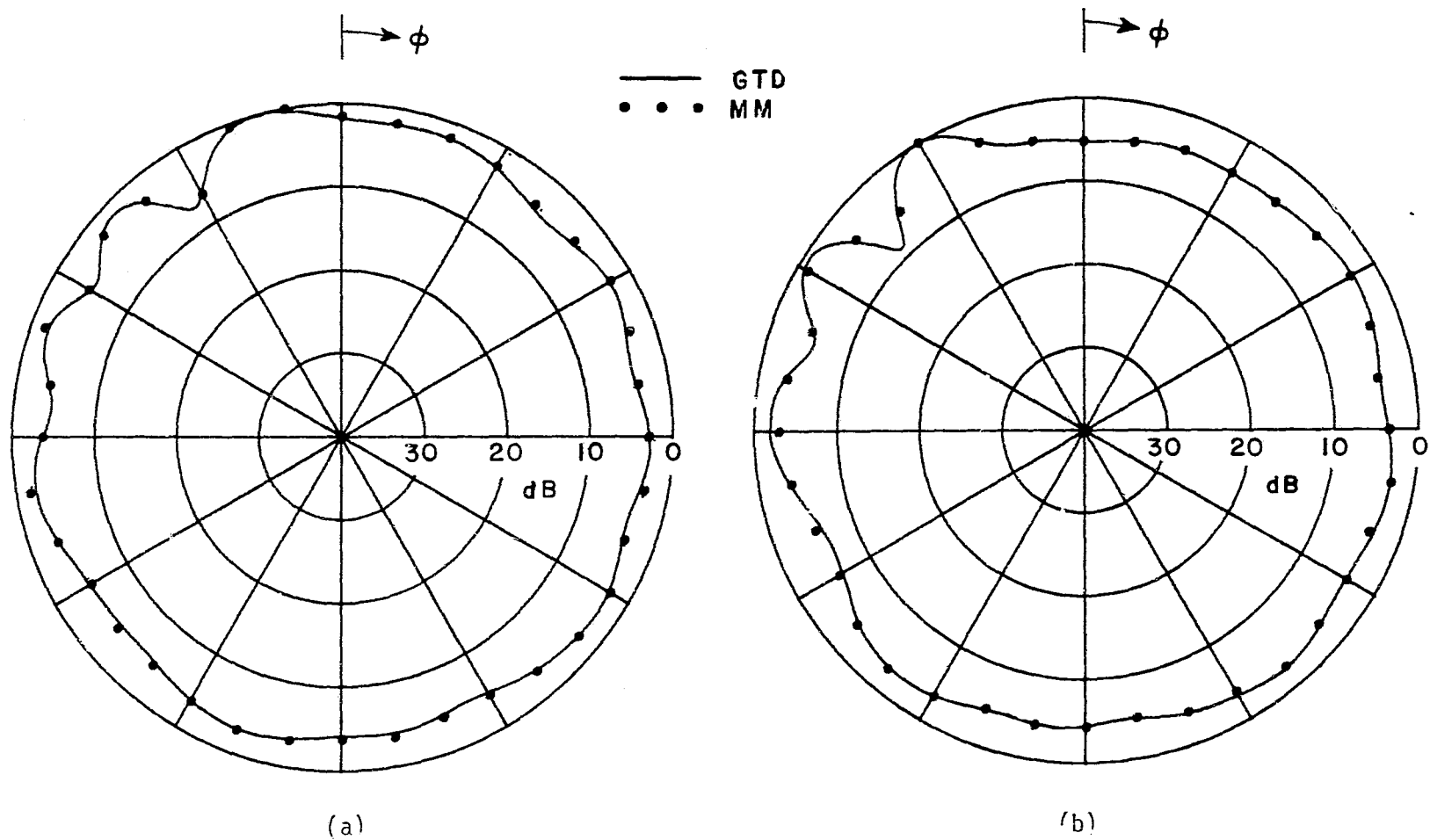


Figure 47. GTD-MM comparison with electric line source and carrying ϕ_s , using geometry shown in Figure 44 with $L=2.2\lambda$, $D=.05\lambda$, $\rho_s=2.2\lambda$. (a) $\phi_s=20^\circ$. (b) $\phi_s=40^\circ$.

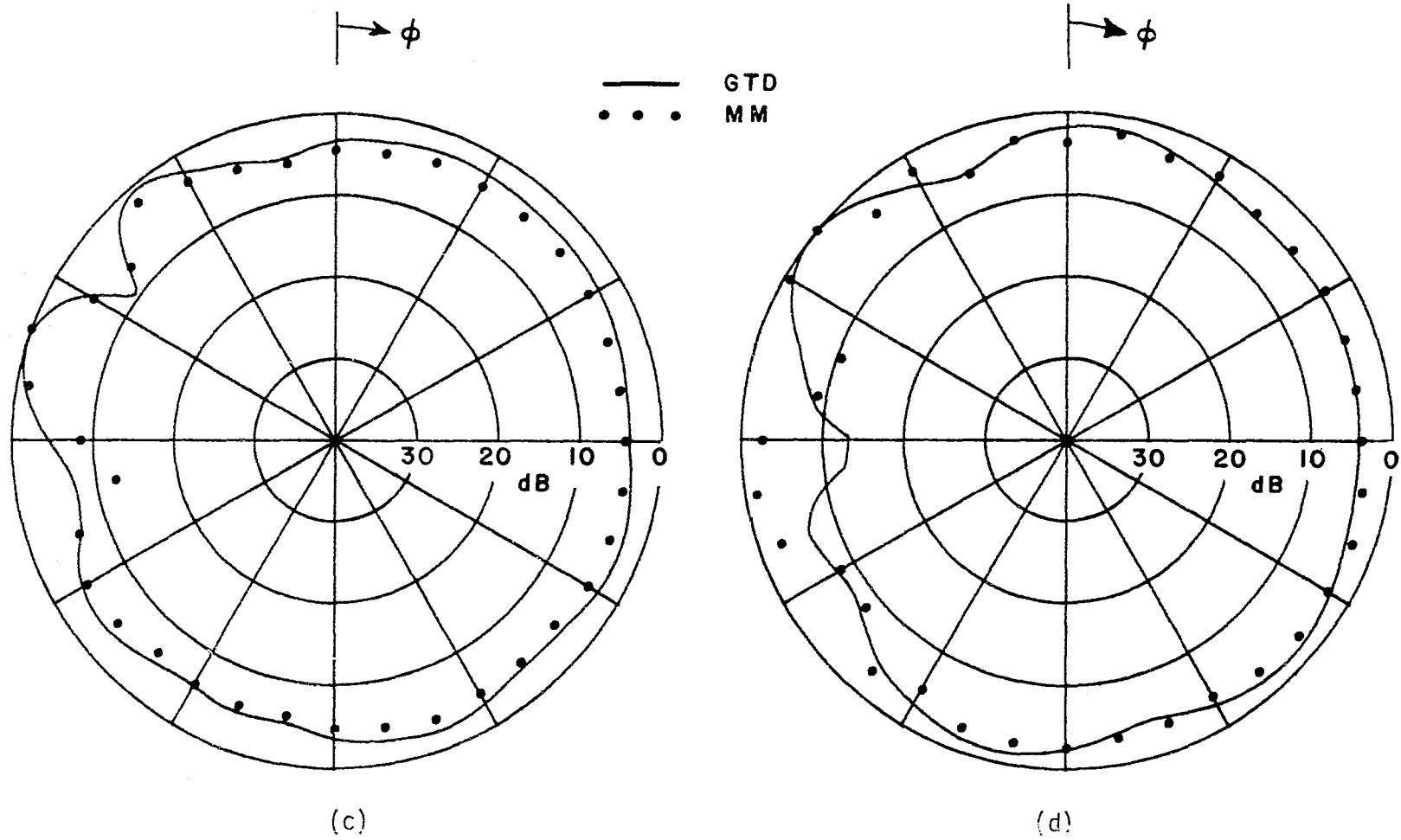


Figure 47. GTD-MM comparison with electric line source and varying ϕ_s , using geometry shown in Figure 44 with $L=2\lambda$, $D=0.05\lambda$, $\rho_s=2\lambda$. (c) $\phi_s=60.0^\circ$. (d) $\phi_s=80.0^\circ$.

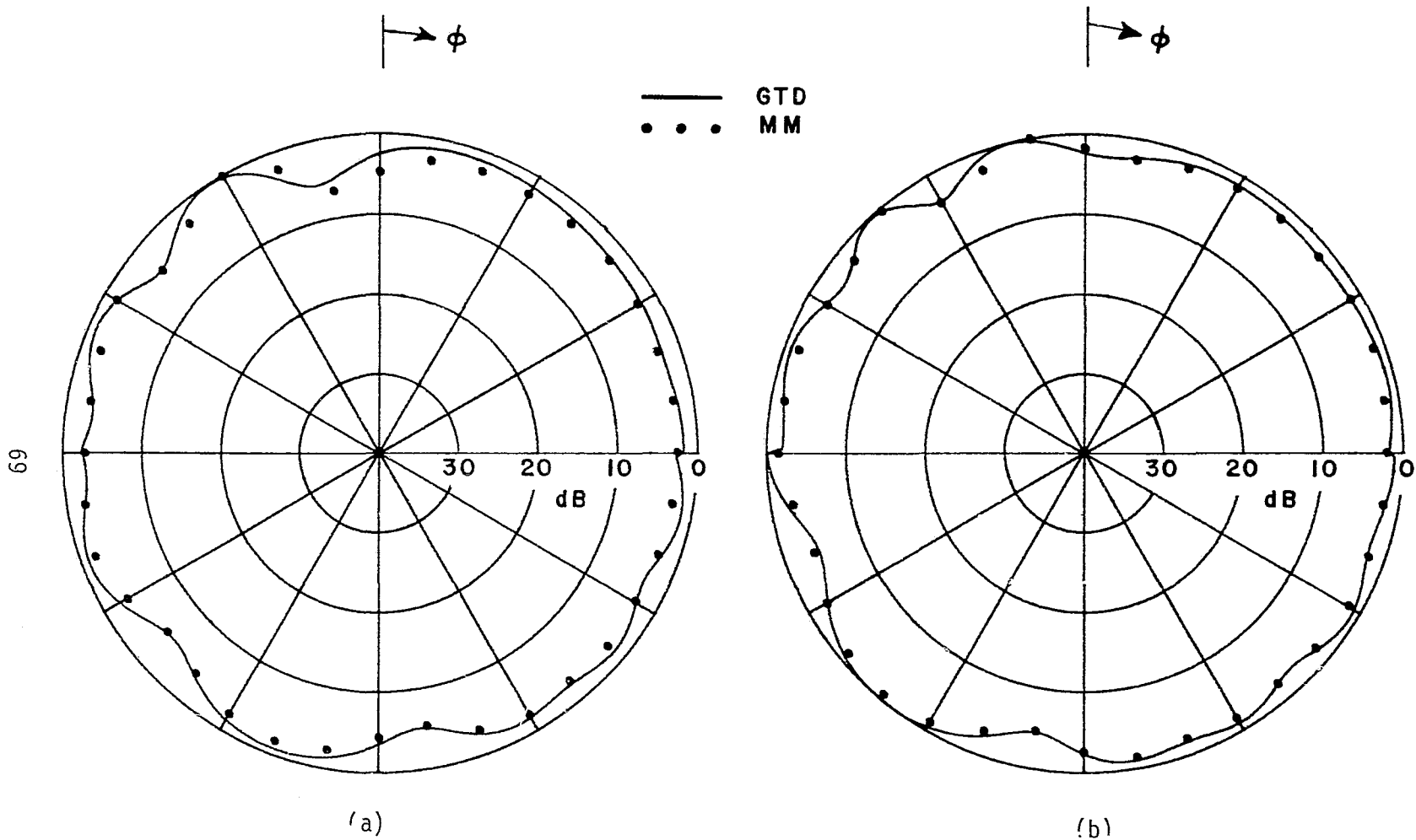


Figure 48. GTD-MM comparison with magnetic line source and varying ϕ_s , using geometry shown in Figure 44 with $L=1.\lambda$, $D=.1\lambda$, $\rho_s=2.\lambda$. (a) $\phi_s=20.^{\circ}$. (b) $\phi_s=40.^{\circ}$.

CHAPTER V CONCLUSIONS

This thesis has demonstrated that geometrical optics and the Geometrical Theory of Diffraction can be modified to include scattering from thin dielectric slabs. Thus it will soon be possible to model structures such as private aircraft in which non-metallic parts play a significant role. This approach will provide efficient computation of a volumetric antenna pattern and is expected to give reasonable accuracy.

The limitations on the application of this theory are not severe, but must be noted. As shown in the Moment Method comparisons, the source must be kept at least a wavelength or so away from the dielectric to keep within the plane wave approximation of Chapter II. The angle of incidence, i.e., the angle between the incident ray and the normal to the dielectric layer, must be kept to not much greater than 60° or so to avoid exciting a surface wave, which was assumed not significant in Chapter II. An additional limitation is on the thickness of the dielectric. The theory was developed on the assumption of the thickness being less than one tenth wavelength; however, accurate results have been obtained for dielectrics with thickness of nearly one half wavelength in free space based on comparisons with measurements.

The question of diffractions from the junction of a dielectric slab and a metal plate or two dielectric slabs remains unanswered, but it is expected that a solution is available by the same methods presented here. Derivation of this would then provide the total theory needed for full incorporation in an aircraft antenna code.

REFERENCES

1. A. Sommerfeld, Optics, Academic Press, Inc., New York, 1954, pp. 245-265.
2. W. Pauli, "An Asymptotic Series for Functions in the Theory of Diffraction of Light," Phys. Rev., 54, (1 December 1938), pp. 924-931.
3. J. B. Keller, "Geometrical Theory of Diffraction," J. Opt. Soc. Am., 52, pp. 116-130, 1962.
4. D. L. Hutchins and R. G. Kouyoumjian, "A New Asymptotic Solution to the Diffraction by a Wedge," URSI, 1967 Spring Meeting; Ottawa, Canada, pp. 154-155.
5. K. W. Burgener and W. D. Burnside, "Analysis of Private Aircraft Antenna Patterns," Report 710964-2, January 1979, The Ohio State University ElectroScience Laboratory, Department of Electrical Engineering; prepared under Grant NSG 1498 for National Aeronautics and Space Administration, Langley Research Center.
6. E. Jordan, Electromagnetic Waves and Radiating Systems, Prentice-Hall, Inc., Englewood Cliffs, New Jersey (1950), pp. 135-141.
7. R. G. Kouyoumjian and P. Pathak, "A Uniform Geometrical Theory of Diffraction for an Edge in a Perfectly Conducting Surface," Proceedings of the IEEE, Volume 62, No. 11, November 1974, pp. 1448-1461.
8. R. G. Kouyoumjian and P. H. Pathak, "The Dyadic Diffraction Coefficient for a Curved Edge," Report 3001-3, August 1973, The Ohio State University ElectroScience Laboratory, Department of Electrical Engineering; prepared under Grant NGR 36-008-144 for NASA, Langley Research Center, Hampton, Va.
9. P. M. Russo, R. C. Rudduck, and L. Peters, Jr., "A Method for Computing E-Plane Patterns of Horn Antennas," IEEE Trans. on Antennas and Propagation, AP-13, No. 2, March 1965, pp. 219-224.

10. J. H. Richmond, "Scattering by a Dielectric Cylinder of Arbitrary Cross Section Shape," IEEE Trans. on Antennas and Propagation, AP-13, No. 3, May 1965, pp. 334-341.
11. J. H. Richmond, "TE-Wave Scattering by a Dielectric Cylinder of Arbitrary Cross-Section Shape," IEEE Trans. on Antennas and Propagation, AP-14, No. 4, July 1966, pp. 460-464.